

1

Snow Interception Relationships with 2 Meteorology and Canopy Density in a 3 Subalpine Forest

4

5 **Authors:**

6 Alexander Charles Cebulski¹ (ORCID ID - 0000-0001-7910-5056)

7 John Willard Pomeroy¹ (ORCID ID - 0000-0002-4782-7457)

8 ¹Centre for Hydrology, University of Saskatchewan, Canmore, Canada

9 **Corresponding Author:** A.C. Cebulski, 50 Lincoln Park, Canmore, Alberta, Canada, T1W

10 3E9, alex.cebulski@usask.ca

11 **Abstract:** Snow accumulation models differ in how snow interception and ablation processes
12 are represented and thus their application to diverse climates and forest types is uncertain.
13 Existing parameterizations of initial snow interception before unloading include inherently
14 coupled canopy snow accumulation and ablation processes. This leads to difficulty in di-
15 agnosing processes and adding possible errors to simulations when incorporated as canopy
16 interception routines in models that already account for canopy snow ablation. This study
17 evaluates the theory underpinning parameterizations of initial snow interception using high-
18 temporal resolution and fine-scale measurements of throughfall for events with minimal snow
19 ablation and redistribution in both the canopy and on the ground. The relationship between
20 these throughfall measurements, event meteorology, and a novel lidar-based canopy density
21 measurement are assessed in two subalpine forest plots in the Canadian Rockies. Contrary

22 to existing theories, no association of canopy snow load or air temperature with interception
23 efficiency was observed. Instead, canopy density emerged as the primary factor governing
24 snow accumulation. A wind-driven snowfall event demonstrated that non-vertical hydrome-
25 teor trajectories can significantly increase snow-leaf contact area, thereby enhancing initial
26 interception before ablation. Prediction of interception efficiency for this event improved dra-
27 matically when adjusted for hydrometeor trajectory angle based on a wind speed at one-third
28 of the canopy height. Snow-leaf contact area showed a high sensitivity to wind speed, increas-
29 ing by up to 95% with a 1 m s^{-1} wind speed. The study proposes a new parameterization
30 that calculates throughfall, independent of processes that ablate snow from the canopy, as a
31 function of snowfall, canopy cover, and above canopy wind speed. This new parameterization
32 successfully estimated subcanopy snow accumulation for a snowfall event at two forest plots
33 measured using lidar and snow surveys. By separating canopy snow ablation from snow inter-
34ception processes, this new model offers potentially improved prediction of subcanopy snow
35 accumulation when combined with canopy snow ablation parameterizations.

36 **Keywords:** snow interception, throughfall, ablation, forest, snowpack, lidar, process-based
37 modelling

38 1 Introduction

39 Over half of North America's snow-covered zone is covered by forests (Kim et al., 2017), signif-
40 icantly impacting the accumulation and redistribution of snowpacks and subsequent snowmelt
41 runoff. Essery et al. (2003) estimated that 25–45% of annual snowfall may be lost to the atmo-
42 sphere due to sublimation of snow intercepted in forest canopies globally. Snow intercepted
43 in the canopy can sublimate and melt at much higher rates than the subcanopy snowpack
44 (Katsushima et al., 2023; Lundberg & Halladin, 1994; Pomeroy et al., 1998), reducing the
45 amount of snow available for runoff. Vegetation structure is one of the primary factors con-
46 trolling the partitioning of snowfall into throughfall and interception (Hedstrom & Pomeroy,
47 1998; Storck et al., 2002), and thus governs the quantity of snow subject to sublimation from

48 the canopy. However, forest thinning efforts aimed at limiting sublimation losses to increase
49 snowmelt runoff do not always lead to a corresponding increase in spring streamflow (Golding
50 & Swanson, 1978; Harpold et al., 2020; Pomeroy et al., 2012; Troendle, 1983). This may be
51 due to increased ablation rates when forest cover is reduced, desynchronization of snowmelt,
52 and sub-surface hydrology interactions (Ellis et al., 2013; Musselman et al., 2015; Pomeroy et
53 al., 1997; Safa et al., 2021; Varhola et al., 2010). Given the significant impact of forest cover
54 on snowpacks, along with the limited or absent monitoring networks for subcanopy snow accu-
55 mulation (Rittger et al., 2020; Vionnet et al., 2021), land management, ecological conservation,
56 and water resource decisions depend on reliable models of snow redistribution.

57 Hedstrom & Pomeroy (1998), working in the cold continental boreal forest, proposed that
58 initial snow interception efficiency was controlled by the maximum canopy load which itself
59 was a function of leaf area index and new snow density. Unloading was found to be an ex-
60 ponential function of time that was observed only days or weeks after the interception event.
61 Storck et al. (2002), working in temperate coastal forests, emphasized the role of leaf area
62 index and air temperature in controlling the maximum canopy snow load. Gelfan et al. (2004)
63 demonstrated accurate subcanopy snowpack simulations at study sites in Russia by treating
64 the Hedstrom & Pomeroy (1998) and Storck et al. (2002) parameterizations separately while
65 using a step-based function to choose either parameterization based on air temperature. A
66 similar parameterization in the Cold Regions Hydrological Model (Pomeroy et al., 2022) has
67 shown strong performance at sites across Canada, northern United States, Switzerland, and
68 Spain. However, overestimation of subcanopy snow accumulation was reported by Lundquist
69 et al. (2021) and Lumbrazo et al. (2022) when combining the Hedstrom & Pomeroy (1998)
70 routine with ablation parameterizations from different studies (e.g., Roesch et al., 2001). The
71 coupling of ablation processes within existing snow interception models (Hedstrom & Pomeroy,
72 1998; Storck et al., 2002) may contribute to overestimates of throughfall, canopy snow unload-
73 ing, and canopy snow melt when combined with other canopy snow ablation parameterizations
74 (Cebulski & Pomeroy, 2025). Additional observations of snow interception that exclude abla-
75 tion processes could help determine the applicability of the interception theories proposed by

76 Hedstrom & Pomeroy (1998) and Storck et al. (2002). Hedstrom & Pomeroy's (1998) theory
77 also suggests that moderate wind speeds, which can result in more horizontal hydrometeor tra-
78 jectories, increasing snow-leaf contact area and interception efficiency at the plot scale. This
79 association has also been shown in rainfall interception studies to decrease throughfall of rain
80 (Herwitz & Slye, 1995; Van Stan et al., 2011). However, the relationship proposed by Hed-
81 strom & Pomeroy (1998), is typically not included in snow accumulation models as empirical
82 testing of this relationship is lacking.

83 The objective of this paper is to evaluate the theories underlying existing snow interception
84 models using high spatial and temporal resolution measurements of subcanopy snow accumu-
85 lation for events with minimal canopy snow ablation. These new observations are investigated
86 to address the following research questions:

- 87 1. Are the existing theories regarding the relationships between meteorology and forest
88 structure and initial snow interception supported by in-situ observations collected in the
89 Canadian Rockies?
- 90 2. Is snow interception influenced by non-vertical hydrometeor trajectory angles over a
91 wind-driven snowfall event?
- 92 3. To what extent can these findings inform the development of a new parameterization for
93 snow interception?

94 **2 Theory**

95 **2.1 Canopy snow mass balance**

96 The change in canopy snow load over time, $\frac{dL}{dt}$ (mm s^{-1}), can be estimated from the mass
97 balance:

$$\frac{dL}{dt} = [q_{sf} - q_{tf} + q_{ros}] - q_{unld} - q_{drip} - q_{wind}^{veg} - q_{sub}^{veg} \quad (1)$$

98 where q_{sf} is the snowfall rate (mm s^{-1}), q_{ros} (mm s^{-1}) is the rate of rainfall falling on snow
 99 intercepted in the canopy, q_{tf} (mm s^{-1}) is the throughfall rate (mm s^{-1}), q_{unld} is the canopy
 100 snow unloading rate (mm s^{-1}), q_{drip} is the canopy snow drip rate due to canopy snowmelt (mm
 101 s^{-1}), q_{wind}^{veg} is the wind transport rate in or out of the control volume (mm s^{-1}), and q_{sub}^{veg} is the
 102 intercepted snow sublimation rate (mm s^{-1}). Figure 1 in Cebulski & Pomeroy (2025) presents
 103 a visual representation of this mass balance.

104 Interception efficiency, $\frac{I}{P}$ (-), which is the fraction of snowfall intercepted over Δt before
 105 ablation, can be calculated as:

$$\frac{I}{P} = \frac{\Delta L}{q_{sf}\Delta t} \quad (2)$$

106 During periods with low air temperatures and low wind speeds, q_{ros} , q_{unld} , q_{drip} , q_{wind}^{veg} , and
 107 q_{sub}^{veg} can be assumed negligible and thus the right side of Equation 1 can be simplified and
 108 used as an approximation of ΔL to calculate $\frac{I}{P}$ as:

$$\frac{I}{P} = \frac{(q_{sf} - q_{tf})\Delta t}{q_{sf}\Delta t} \quad (3)$$

109 2.2 Hydrometeor trajectory angle

110 Herwitz & Slye (1995) calculate the trajectory angle of a hydrometeor, θ_h , as the departure in
 111 degrees ($^\circ$) from a vertical plane as:

$$\theta_h = \arctan \left(\frac{x_h(u_z)}{v_h(D_h)} \right) * \frac{180}{\pi} \quad (4)$$

112 where $v_h(D_h)$ is the terminal fall velocity of the hydrometeor (m s^{-1}), which is a function of
 113 the hydrometeor diameter, D_h and $x_h(u_z)$ is the horizontal velocity of the hydrometeor (m
 114 s^{-1}) which is a function of the within canopy wind speed, u_z at height above ground, z . In
 115 the absence of hydrometeor velocity observations, $v_h(D_h)$ may be approximated from values

in the literature (e.g., 0.8 m s^{-1} in Isyumov (1971)) and $x_h(u_z)$ can be approximated by the above canopy horizontal wind speed. This assumes the hydrometeors are following fluid points in the atmosphere.

3 Data and methods

3.1 Study site

This study was conducted at Fortress Mountain Research Basin (FMRB), Alberta, Canada, -115° W , 51° N , a continental headwater basin in the Canadian Rockies (Figure 1). Data from this study was collected between October 2021 and July 2023 within and surrounding two forest plots adjacent to the FMRB Powerline Station (PWL) and Forest Tower Station (FT) at $\sim 2100 \text{ m}$ above sea level as shown in Figure 1. The average annual precipitation at PWL Station from 2013 to 2023 was 1045 mm, with the peak annual snow water equivalent (SWE) reaching 465 mm, typically occurring in late April. The PWL plot is adjacent to PWL station and the FT plot surrounds FT station and both include discontinuous stands of 70% subalpine fir (*Abies lasiocarpa*) and 30% Engelmann spruce (*Picea engelmannii*) (Langs et al., 2020). The canopy closure of the two forest plots are 0.51 and 0.29 and the winter leaf area indices are 2.07 and 1.66 for PWL and FT respectively. The average height of the canopy within the PWL plot is 10.5 m and within the FT plot is 7.1 m. In August of 1936, the majority of vegetation in FMRB burned during a large forest fire that affected most of the Kananaskis Valley (Fryer et al., 1988). Following the fire, the forest within the PWL and FT forest plots has naturally regenerated, though some trees have been removed for road clearing and creation of a snow study plot.

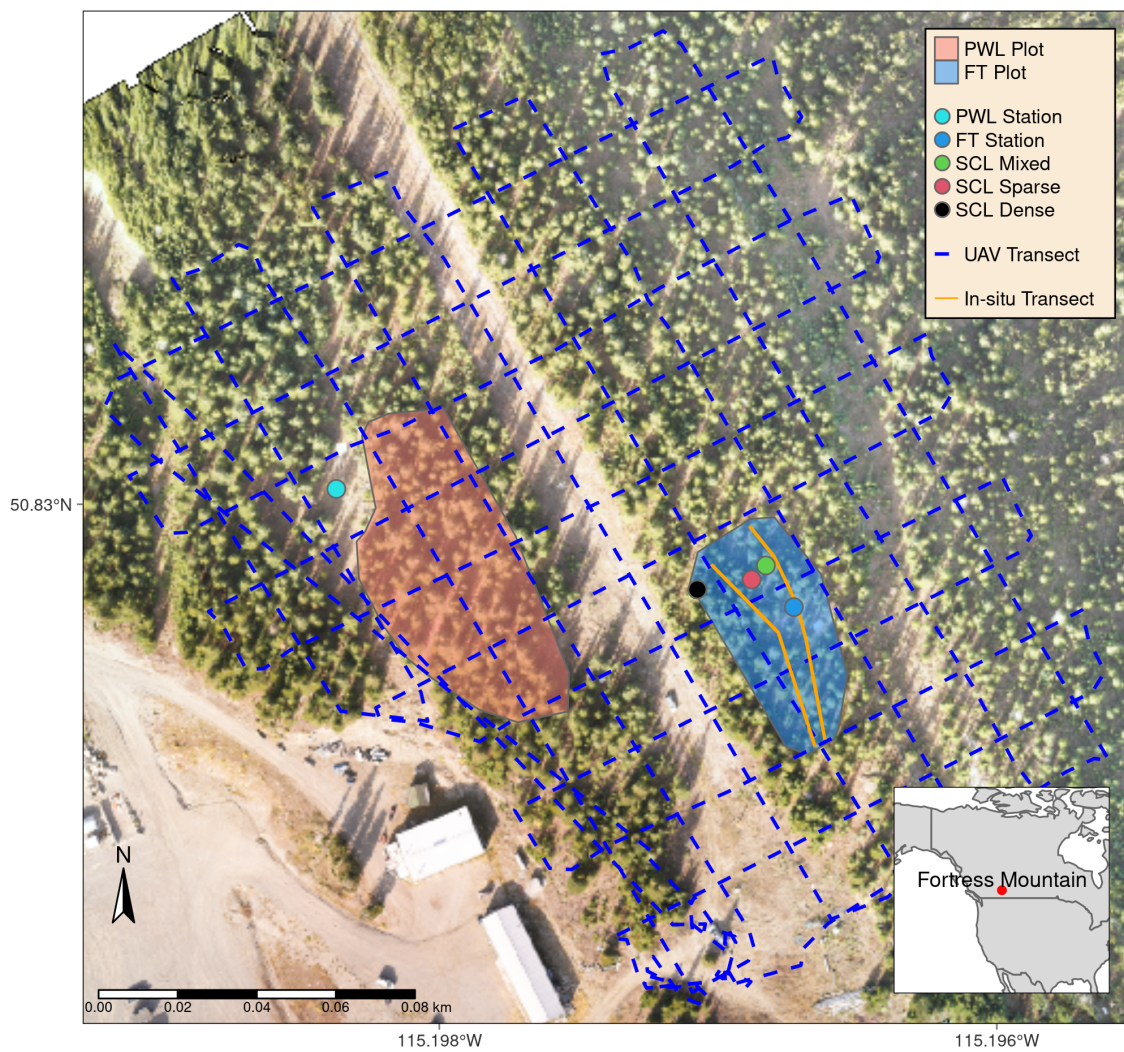


Figure 1: Map showing the location of forest plots, flux towers, subcanopy lysimeter instruments (SCL), and survey transects. The inset map on the lower right shows the regional location of Fortress Mountain Research basin.

¹³⁷ **3.2 Meteorological measurements**

¹³⁸ Measurements of air temperature and relative humidity (Vaisala model HMP155A), wind speed
¹³⁹ and direction (RM Young model 86000 2-D ultrasonic anemometer) were made 4.3 m above the
¹⁴⁰ ground at FT station (Figure 1). Wind speed measurements from a 3-cup anemometer (Met
¹⁴¹ One model 014A), installed adjacent to the 2-D ultrasonic anemometer at 4.3 m, were used to
¹⁴² fill data gaps in the 2-D ultrasonic anemometer records. Additional wind speed measurements
¹⁴³ were collected by two 3D sonic anemometers (Campbell Scientific CSAT3) installed at 2 m
¹⁴⁴ (raised to 3 m February 2022) and 13.5 m above the ground at FT station. Average wind speeds
¹⁴⁵ at these three heights were found to follow a logarithmic relationship. Thus, a wind profile
¹⁴⁶ was fitted to these measurements using the Prandtl-von Kármán log-linear relationship:

$$\bar{u} = \frac{u_*}{k} \ln\left(\frac{z - d_0}{z_0}\right) \quad (5)$$

¹⁴⁷ where \bar{u} is average wind speed (m s^{-1}) at height, z (m) above the ground, u_* is the friction
¹⁴⁸ velocity (m s^{-1}), d_0 is the displacement height (m), z_0 is the roughness length of momentum
¹⁴⁹ (m), and k is the dimensionless von Kármán Constant (0.4).

¹⁵⁰ Using wind speed measurements at three heights at FT station, collected during events when
¹⁵¹ the instruments were confirmed to be free of snow, the function ‘optim’ from the ‘stats’ R
¹⁵² package (R Core Team, 2024) was used to estimate the values d_0 and z_0 for Equation 5 that
¹⁵³ best fit the observed mean wind speed. The parameters found for the wind speed profile
¹⁵⁴ include a d_0 of 0.58 m and z_0 of 0.50 m. See the supporting information for more information
¹⁵⁵ on the development and testing of the wind profile.

¹⁵⁶ At PWL station, the snowfall rate was measured by an Alter-shielded OTT Pluvio weighing
¹⁵⁷ precipitation gauge 2.6 m above ground, corrected for undercatch following phase correction
¹⁵⁸ by Harder & Pomeroy (2013) and catch efficiency by Smith (2007). The instrument accuracy
¹⁵⁹ of the OTT Pluvio specified in the instrument manual is +/- 0.1 mm or 0.2% (whichever is
¹⁶⁰ larger). Wind speed for undercatch correction was measured by a 3-cup anemometer (Met One

model 014A) at a height of 2.6 m at PWL station. An optical disdrometer (OTT Parsivel2) provided measurements of hydrometeor particle size and vertical velocity. All measurements were recorded at 15-min intervals using Campbell Scientific dataloggers, except the Parsivel2 which was recorded at 1-minute intervals by an onsite computer.

3.3 Lysimeter measurements

Three subcanopy lysimeters (SCLs) were installed surrounding the FT Station (Figure 1) to provide 15-minute interval measurements of throughfall as in MacDonald (2010). For 26 distinct snowfall events, where canopy snow ablation rates were deemed negligible, snow captured in the SCLs was determined to be predominantly from throughfall with some contribution of canopy snow unloading. Timelapse imagery, mass change on a weighed tree lysimeter “hanging tree” (Pomeroy & Schmidt, 1993), and in-situ observations were used to ensure the unloading of canopy snow was minimal over each interval. Additionally, the throughfall measurements were filtered to include observations that coincided with a snowfall rate $> 0 \text{ mm hr}^{-1}$, throughfall rate $> 0.05 \text{ mm hr}^{-1}$, and where snowfall exceeded the SCL measured throughfall rate. Rates of q_{ros} , q_{drip} , and q_{wind}^{veg} were observed to be zero for these periods. While these careful manual mitigation and automated filtering strategies substantially reduce the contribution of unloading in the SCL throughfall measurements, a small contribution is still possible.

The throughfall rate, q_{tf} , was calculated by dividing the weight of snow in the SCL by the cross-sectional area of the SCL opening and determining the rate of change at 15-minute intervals. Figure 2 shows the three SCLs which consisted of a plastic horse-watering trough with an opening of 0.9 m^2 and depth of 20 cm suspended from a load cell (Intertechnology 9363-D3-75-20T1) attached to an aluminum pipe connected between two trees. The manufacturer-specified combined error of the load cells is $+/- 0.02\%$ and a temperature sensitivity of $+/- 0.001\%/5^\circ\text{C}$. The SCLs were installed in locations selected to limit preferential throughfall and unloading by choosing locations with relatively continuous canopy (e.g., avoiding forest edges) and away from large branches which could preferentially unload snow. The mixed canopy

SCL had a slight canopy opening, shown in Figure 2, orientated towards the prevailing wind direction observed during the study period which allowed some preferential measurement of throughfall for snowfall trajectories aligned with this gap. The canopy surrounding the SCLs led to reduced wind speeds and reduced the potential for gauge undercatch. Canopy snow load was estimated at the same 15-minute intervals during these events using Equation 1 and incorporating measurements of q_{tf} from the SCLs and q_{sf} from the PWL snowfall gauge. Interception efficiency was also calculated for these intervals using Equation 3. Photographs of the three SCLs and surrounding canopy density are shown in Figure 2. The leaf area index and canopy closure for each SCL are presented in Table 1. A viewing angle of 60° from zenith was selected to describe the SCLs in the results section as non vertical hydrometeor trajectory angles were expected to influence the measurements at these locations. These canopy density metrics were measured using hemispherical photography (Nikon Coolpix 4500 and EC-F8 hemispherical lens) and analyzed with the hemispheR R package Chianucci & Macek (2023).

The weighed tree lysimeter, a live subalpine fir (*Abies lasiocarpa*) tree suspended from a load cell (Artech S-Type 20210-100) measured the weight of canopy snow load (kg). This weight was scaled to an areal estimate of canopy snow load (L , mm) using measurements of areal throughfall (mm) from in-situ snow surveys and snowfall from the PWL Station snowfall gauge (see description of method in Pomeroy & Schmidt, 1993). Although the weighed tree lysimeter provides a more direct measurement of canopy snow load compared to the SCLs, it was not used in the interception efficiency calculation as variations in the trees mass may be attributed to canopy snow sublimation, unloading and melt. Since the subcanopy lysimeter estimates of canopy snow load are not influenced by sublimation, they provide a measurement of I/P with less uncertainty.

Table 1: Canopy density of the three subcanopy lysimeters (SCL) located proximal to the FT Station. Leaf area index (LAI) and canopy closure was measured using hemispherical photo analysis for varying viewing angles from zenith.

Name	Angle From Zenith (°)	LAI (-)	Canopy Closure (-)
Sparse	15	0.45	0.19
Sparse	30	1.12	0.44
Closed	15	1.58	0.54
Sparse	45	1.43	0.56
Mixed	15	2.00	0.63
Sparse	60	1.56	0.64
Closed	30	2.01	0.65
Mixed	30	2.34	0.71
Mixed	45	2.33	0.74
Mixed	60	2.10	0.75
Closed	45	2.47	0.76
Closed	60	2.40	0.79

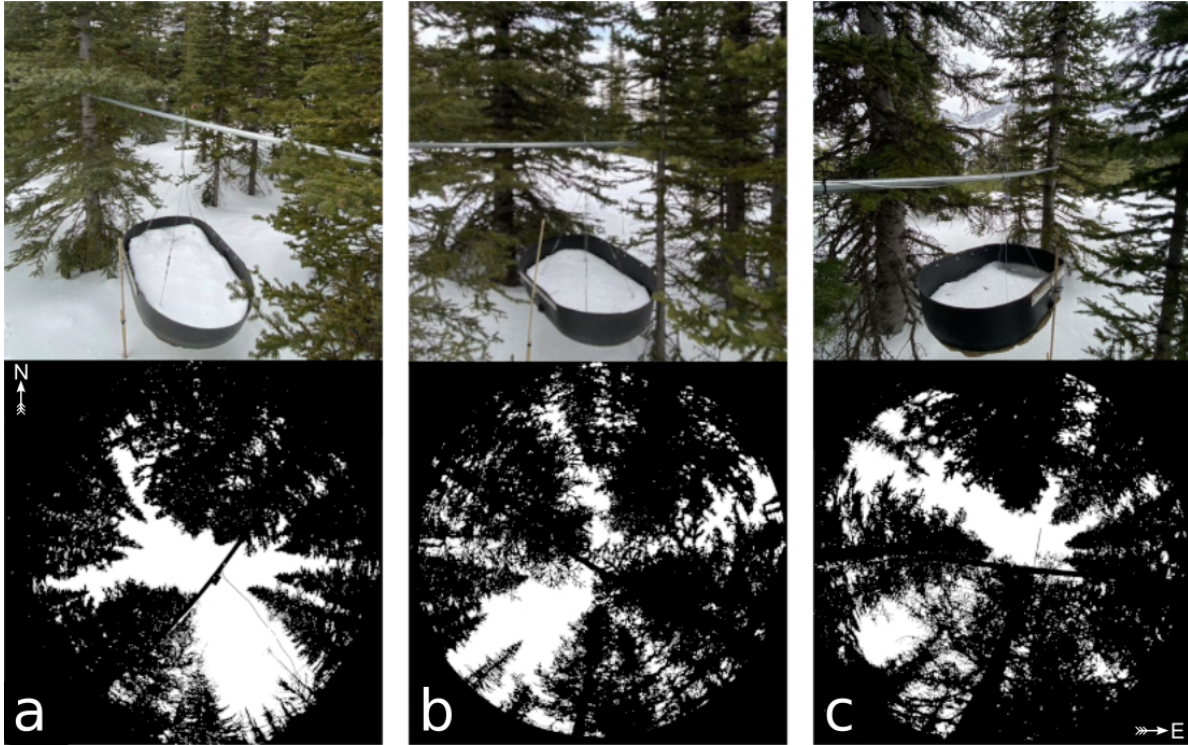


Figure 2: Images of the three subcanopy lysimeters (SCL) and surrounding canopy located in sparse (a), mixed (b), and dense (c) canopy. The top row presents a side view of each SCL and the bottom row shows hemispherical photographs classified using the hemispheR R package. These hemispherical images are oriented with north at the top and have been mirrored to provide a view from above (e.g., east is on the right side of each image). See Table 1 for the canopy density measurements above each SCL.

3.4 UAV-Lidar data collection and processing

The UAV (FreeFly Alta X) payload included a REIGL miniVUX-2 airborne laser scanner, an Applanix APX-20 inertial measurement unit (IMU) and global navigation satellite system (GNSS). The UAV was flown 90 m above the ground at a speed of 3 m s^{-1} following the path shown in Figure 1. The methods outlined by Harder et al. (2020) and Staines & Pomeroy (2023) were incorporated to reconcile survey lidar, IMU and GNSS data. A systematic vertical bias of up to 6 cm between UAV-lidar flight lines was observed in the resulting point clouds

on March 13th and 14th, 2024 and was attributed to IMU position drift. After strip alignment, the mean elevation bias in the point clouds compared to the GNSS data was 0.000 m and the RMS error declined from 0.055 m to 0.038 m on March 13th and changed from 0.033 m to 0.029 m on March 14th. The point cloud density ranged from ~1200 returns m² in sparse forest to ~2200 returns m² in open clearings. Quality control, ground classification, calculation of surface elevation change was conducted on the point cloud data and then converted to 0.05 m resolution rasters. Further quality control was conducted on the 0.05 m raster data to remove values that exceeded the .999th quantile and then resampled to 0.25 m grid cell resolution by taking the median. A detailed description of the UAV, payload, flight settings, and software packages used is provided in the supporting information.

3.5 Snow surveys

3.5.1 In-situ snow depth and density

Event-based snow surveys provided measurements of subcanopy throughfall depth and density at 30 locations following the transects shown in Figure 1. These measurements were used to upscale the weighed tree from kg to kg m⁻², assess the accuracy of lidar derived snow depth measurements, and provide a fresh snow density for the calculation of SWE (mm). Minimal ablation and redistribution of both the surface snowpack and/or snow intercepted in the canopy was crucial to ensure the snow survey measurements were attributed to throughfall. Therefore, only snowfall events with minimal canopy snow ablation as determined through in-situ observations, analysis of timelapse imagery, and mass change on the weighed tree lysimeter were selected. Twelve select in-situ fresh snow surveys (six pre- and post-snowfall event pairs) conducted between January and May were used to upscale the weighed tree from kg to kg m⁻². In-situ snow surveys were also conducted following the UAV-lidar flights on March 13th and March 14th. A 1000 cm³ Perla snow density wedge sampler (RIP Cutter, <https://snowmetrics.com/shop/rip-1-cutter-1000-cc/>) was used to measure the density of the

243 fresh snow layer, $\overline{\rho_{tf}}$ (kg m^{-3}) from snow pits. Throughfall depth measurements, ΔHS were
244 converted to SWE using the following equation:

$$\Delta SWE_{tf} = \Delta HS \cdot \overline{\rho_{tf}} \quad (6)$$

245 If a pre-event crust layer was present, the depth of post event fresh snow accumulation above
246 the crust layer was interpreted as throughfall over the event. In the absence of a defined crust
247 layer, the difference in pre- and post-event snow depth to ground was interpreted as event
248 throughfall.

249 **3.5.2 UAV-Lidar snow depth**

250 Two uncrewed aerial vehicle (UAV) lidar surveys were conducted before and after a 24-hour
251 snowfall event that occurred between March 13th and March 14th, 2023 to facilitate the mea-
252 surement of snow accumulation and canopy density within the FT and PWL forest plots. This
253 period was selected based on two criteria: 1) it provided sufficient cumulative snowfall to result
254 in a low relative error in UAV-lidar measured throughfall, and 2) minimal snow redistribution
255 and ablation was observed, as confirmed by the SCLs, weighed tree, and time-lapse imagery.
256 The change in surface elevation between the two UAV-lidar point clouds was interpreted as the
257 increase in snow accumulation, ΔHS over the snowfall event. ΔSWE_{tf} was calculated using
258 Equation 6 together with in-situ measurements of $\overline{\rho_{tf}}$. The measurement error of the UAV-
259 lidar derived ΔHS was assessed using the in-situ snow depth observations which is shown in
260 the supporting information. Spatially distributed measurements of $\frac{I}{P}$, were then determined
261 using Equation 3 by using ΔSWE_{tf} as the throughfall component ($q_{tf}\Delta t$) and the snowfall
262 accumulation to the open ($q_{sf}\Delta t$) measured between the two lidar surveys at PWL station.

263 **3.6 UAV-Lidar canopy metrics**

264 The canopy of two UAV-lidar point clouds (March 13th and March 14th) was characterized
265 using the voxel ray sampling (VoxRS) methodology for lidar data analysis, as developed by
266 Staines & Pomeroy (2023). This method was chosen for its ability to provide canopy metrics
267 that are less sensitive to the inherent non-uniform nature of lidar sampling data, which often
268 results from beam occlusion in vegetation and leads to reduced points near the ground. Using
269 this method radiation transmittance, τ (-), was measured across the hemisphere at a 1° step,
270 e.g., azimuth angles (0°, 1°, ..., 359°) and zenith angles (0°, 1°, ..., 90°) for each 0.25 m grid cell
271 within the FT and PWL forest plots. The fraction of snow-leaf contact area per unit area of
272 ground proposed by Hedstrom & Pomeroy (1998), and hereafter called leaf contact area (C_p),
273 was then calculated as:

$$C_p(C_c, \theta_h, L) = 1 - \tau \quad (7)$$

$$C_p(C_c, \theta_h, L) = \begin{cases} 1 - \tau, & \text{if } \theta_h > 0^\circ \\ 1 - \tau \approx C_c, & \theta_h = 0^\circ \end{cases} \quad (8)$$

274 where C_p is a function of the canopy cover C_c , θ_h and L . C_c is the fraction of canopy area
275 to total ground area when viewed from above, which differs from canopy closure, an angular-
276 derived metric usually measured from the ground perspective.

277 To determine how C_p was associated with interception efficiency at different azimuth and
278 zenith angles over the March 13–14 snowfall event, the entire hemisphere at each grid location
279 was considered. The relationship between interception efficiency and C_p was found to be linear
280 and thus the Pearson Correlation Coefficient was used. The ρ_p was computed between a single
281 raster of interception efficiency and each of the 32,760 rasters of C_p measured on March 13th,
282 representing locations across the hemisphere (azimuth [0°, 1°, ..., 359°], zenith angle [0°, 1°, ...,
283 90°]) at 0.25 m grid cells spanning the FT and PWL forest plots.

284 **3.7 Statistics and regression models**

285 Linear and non-linear regression models were developed to assess relationships in the observed
286 data. Linear models were fitted using ordinary least squares regression to analyze two re-
287 lationships: (1) between interception efficiency and meteorological variables and (2) between
288 interception efficiency and leaf contact area. The latter was forced through the origin based on
289 the theoretical justification that the dependent variable should be zero when the independent
290 variable is zero. Kozak & Kozak (1995) noted, the default R^2 value provided for least squares
291 models forced through the origin by many statistical packages can be misleading. Therefore,
292 these R^2 values were adjusted using Equation 10 in Kozak & Kozak (1995). Non-linear models
293 were fitted to investigate the relationship of leaf contact area with simulated trajectory angle
294 using non-linear least squares regression. All statistical analyses were conducted using the R
295 ‘stats’ package (R Core Team, 2024).

296 **4 Results**

297 **4.1 The influence of meteorology on snow interception**

298 Canopy snow load was estimated using the SCLs and weighed tree lysimeter for 26 snowfall
299 events and increased linearly with cumulative event snowfall, showing no evidence of reaching
300 a maximum (Figure 3). Over these events, air temperature ranged from -24.5°C to 1°C,
301 wind speeds at 4.3 m height ranged from calm to 4.6 m s⁻¹ (Table 2), and wind direction
302 was predominately from the southwest during snowfall (Figure 4). Missing canopy snow load
303 measurements in Figure 3 for certain events was caused by damage to the wiring due to animals
304 and heavy snow loads. Some of the the variability in interception rates within and between
305 different events may be attributed to small amounts of canopy snow unloading and melt,
306 which could not be fully accounted for through the manual and automated filtering mitigation
307 strategies for in both the SCL and weighed tree measurements. Additionally, the weighed tree

308 lysimeter was influenced by canopy snow sublimation, which was not directly accounted for in
309 our analysis.

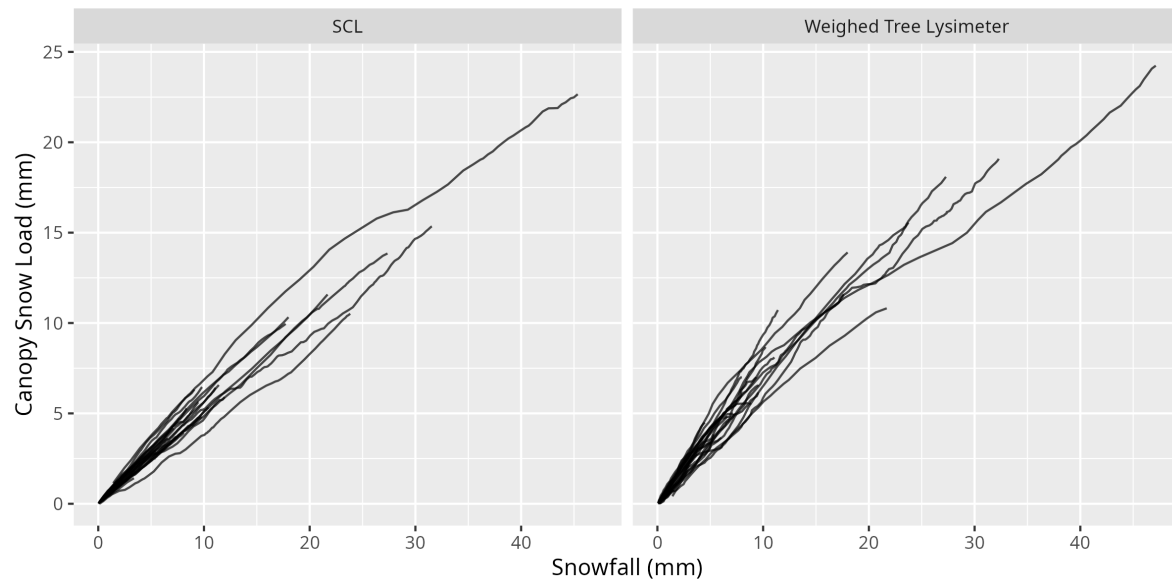


Figure 3: Plot showing the cumulative event snowfall versus the corresponding state of canopy snow load calculated using the average of the three subcanopy lysimeters (SCL, left) and weighed tree lysimeter (right) for each of the 26 snowfall events.

Table 2: Meteorology of the 26 snowfall events. Air temperature and wind speed were measured at FT station. Interception efficiency is estimated from snowfall measured at PWL station and the average throughfall of all three SCLs located within the FT forest plot (all from 15-min. measurements).

Start Date	Air Temperature (°C)			Wind Speed (m/s)			Interception Efficiency (-)			Snowfall (mm)
	Min	Mean	Max	Min	Mean	Max	Min	Mean	Max	
2021-12-23	-6.2	-5.3	-4.6	0.6	3.1	4.6	0.1	0.5	0.9	21.7
2022-01-02	-15.9	-10.8	-5.8	0.2	1.8	4.2	0.0	0.5	1.0	31.6
2022-01-17	-14.8	-7.4	-0.7	0.2	1.1	1.8	0.0	0.5	0.9	12.0
2022-01-31	-24.5	-12.1	-6.4	0.1	1.0	1.7	0.2	0.7	1.0	9.1
2022-02-14	-9.9	-9.0	-8.5	0.4	0.8	1.2	0.2	0.5	0.8	1.7
2022-02-19	-4.7	-3.2	-2.5	1.3	2.3	3.6	0.3	0.6	0.9	11.1
2022-03-01	-8.3	-5.4	-1.0	0.1	1.0	3.1	0.1	0.6	1.0	9.8
2022-03-07	-12.5	-8.5	-3.5	0.3	0.8	1.7	0.0	0.6	1.0	9.5
2022-03-14	-2.7	-2.1	-0.8	1.0	1.6	2.9	0.2	0.6	0.9	8.4
2022-03-19	-3.1	-2.8	-2.5	0.0	0.7	1.3	0.3	0.5	0.6	6.6
2022-03-23	-7.9	-5.3	-0.9	0.8	1.2	1.8	0.4	0.6	0.9	1.6
2022-04-04	-3.5	-2.9	-2.1	0.6	1.0	1.9	0.0	0.4	0.6	3.4
2022-04-18	-5.2	-4.0	-2.7	0.4	1.1	1.9	0.1	0.5	0.9	7.4
2022-04-22	-2.8	-1.8	-0.5	0.4	0.8	1.2	0.1	0.5	1.0	9.8
2022-05-09	-4.9	-4.3	-3.2	0.1	0.4	0.9	0.2	0.5	0.9	8.1
2022-05-19	-4.9	-2.1	0.3	0.1	0.4	0.9	0.2	0.6	0.9	7.1
2022-06-13	-1.1	-0.3	0.6	0.1	0.1	0.4	0.0	0.5	0.9	45.4
2022-12-27	-3.0	-2.7	-1.9	0.6	1.1	1.8	0.2	0.5	0.9	4.5
2023-01-27	-11.5	-7.3	-4.5	0.6	0.9	1.2	0.1	0.5	0.8	10.4
2023-02-19	-14.3	-9.4	-6.3	0.2	0.8	1.4	0.3	0.6	1.0	17.7
2023-02-26	-9.2	-8.4	-6.6	0.2	1.0	2.1	0.3	0.5	1.0	5.4
2023-03-13	-8.9	-3.6	-0.1	0.3	1.3	2.2	0.0	0.5	1.0	27.4
2023-03-24	-7.9	-5.7	-3.5	0.1	0.5	1.2	0.1	0.4	0.7	23.8
2023-04-01	-8.9	-7.7	-4.7	0.1	0.6	1.4	0.4	0.6	0.8	11.4
2023-04-10	-1.1	-0.5	0.3	0.1	0.3	1.0	0.4	0.6	0.8	18.0
2023-05-08	0.2	0.6	1.0	0.4	0.6	0.8	0.5	0.5	0.7	3.5

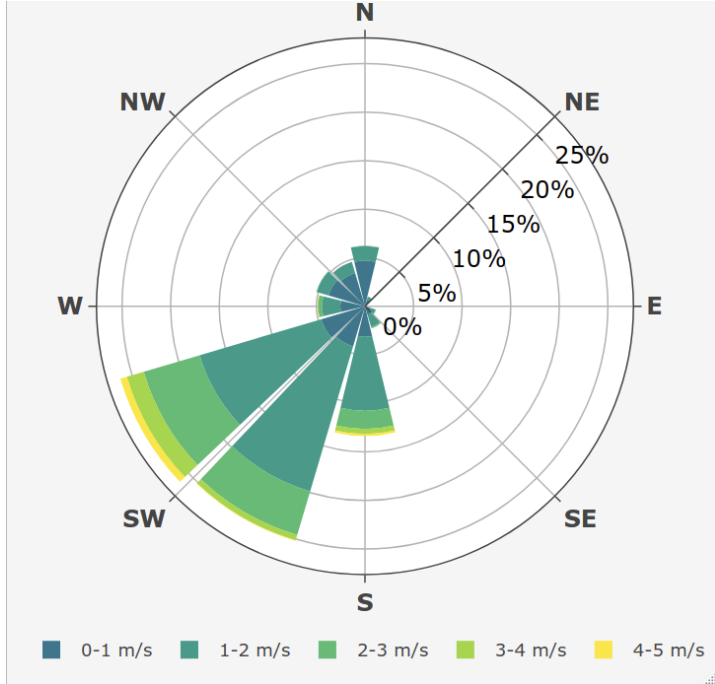


Figure 4: Wind rose showing the frequency of wind speed and direction over the 26 snowfall periods for the ultrasonic anemometer 4.3 m above ground at FT station.

310 Event average air temperature and interception efficiency were negatively associated for the
 311 mixed canopy ($R^2 = 0.1$, $p < 0.05$), but not associated at the closed and sparse canopies
 312 (Table 3 & Figure 5). Cumulative event snowfall was not associated with event interception
 313 efficiency at any site ($p > 0.05$). Event wind speed was positively associated with interception
 314 efficiency for the sparse ($R^2 = 0.1$, $p > 0.05$) and closed ($R^2 = 0.2$, $p < 0.05$) canopies, both
 315 with limited canopy openings (Figure 2a,c) towards the prevailing wind direction shown in the
 316 wind rose in Figure 4. However, interception efficiency in the mixed canopy, which is partially
 317 open towards the prevailing wind direction, was not associated with wind speed ($p > 0.05$).

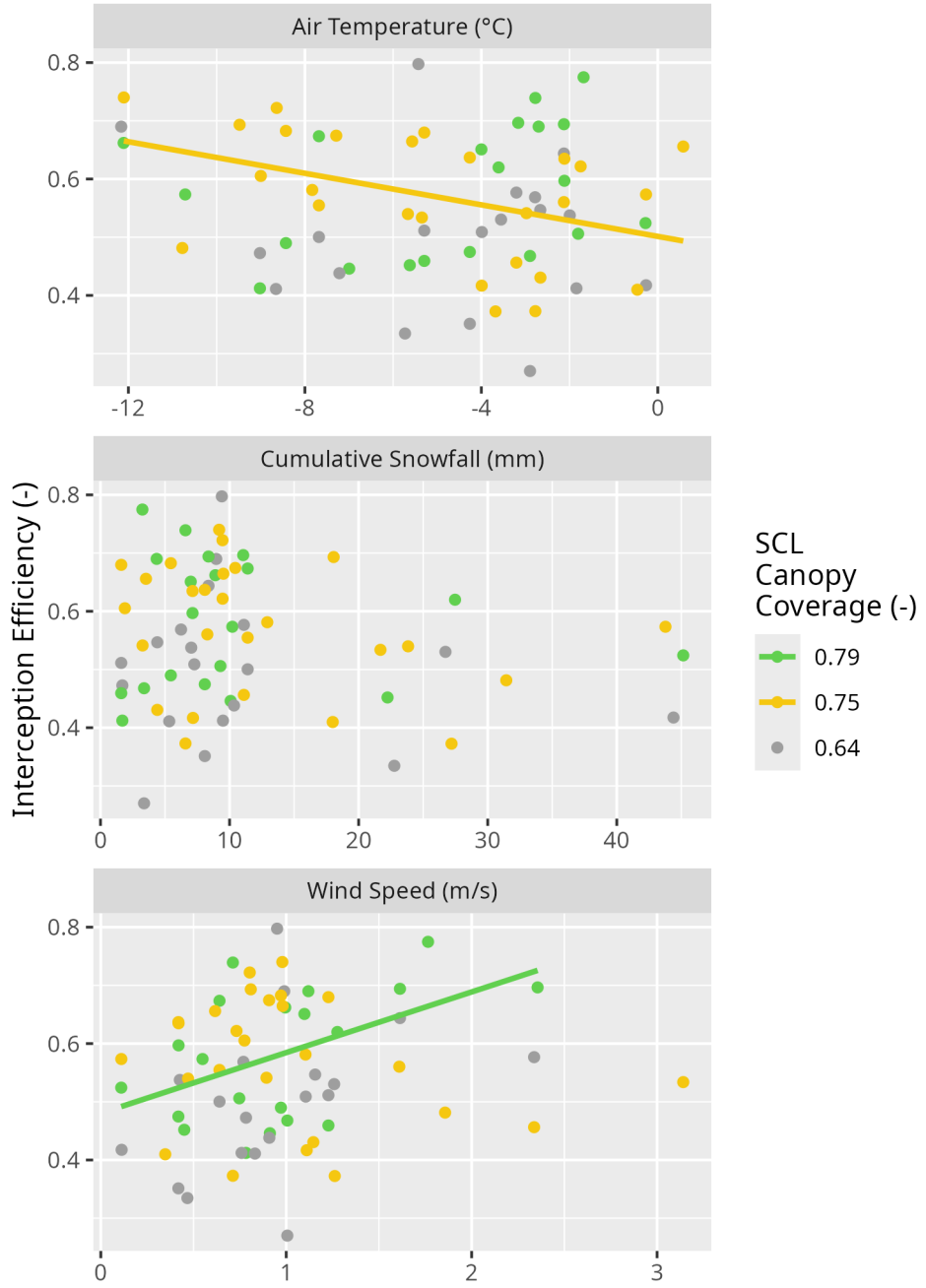


Figure 5: Scatter plots showing the event mean air temperature, mean wind speed, and cumulative snowfall versus the event mean interception efficiency estimated using the SCLs for each of the 26 snowfall events. The colours (grey, yellow, and green), correspond to varying canopy closure (0.64, 0.75, and 0.79). A linear regression line fit to the data for significant relationships ($p < 0.05$) is shown by the solid coloured lines. See Table 3 for linear regression statistics.

Table 3: Statistics corresponding to the ordinary least squares linear regression test between independent variables: mean event air temperature, cumulative event snowfall, and mean event wind speed, and the dependent variable mean event interception efficiency. The test was run separately for three levels of canopy closure (C_c) and for the average of all three SCLs (scl_mean).

SCL					
Dependent Variable	Name	C_c	Adjusted R^2	p-value	n
Air Temperature (°C)	closed	0.79	0.008	0.296	20
Air Temperature (°C)	mixed	0.75	0.141	0.033	26
Air Temperature (°C)	sparse	0.64	-0.033	0.520	19
Air Temperature (°C)	scl_mean	0.73	0.039	0.168	26
Cumulative Snowfall (mm)	closed	0.79	-0.049	0.733	20
Cumulative Snowfall (mm)	mixed	0.75	0.029	0.198	26
Cumulative Snowfall (mm)	sparse	0.64	-0.038	0.569	19
Cumulative Snowfall (mm)	scl_mean	0.73	0.010	0.276	26
Wind Speed (m/s)	closed	0.79	0.192	0.031	20
Wind Speed (m/s)	mixed	0.75	0.010	0.274	26
Wind Speed (m/s)	sparse	0.64	0.114	0.087	19
Wind Speed (m/s)	scl_mean	0.73	-0.020	0.479	26

318 Fifteen-minute interval measurements of interception efficiency and air temperature shown
 319 in Figure 6a were not associated, despite significant relationships for the sparse and mixed
 320 canopies ($R^2 < 0.03$, $p < 0.05$), due to low predictive power (Table 4). The average interception
 321 efficiency across differing bins of air temperature also does not show any systematic trend
 322 (Figure 6a). However, a significantly greater median interception efficiency ($p < 0.05$) was
 323 found for binned measurements with air temperatures below -6 °C compared to those with
 324 warmer air temperatures using non-parametric Wilcoxon signed rank test.

325 Mean wind speed was weakly associated with interception efficiency for the sparse ($R^2 = 0.1$, p
 326 > 0.05) and closed ($R^2 = 0.2$, $p < 0.05$), but not for the mixed canopy ($p > 0.05$) (Table 4). The

327 binned data show an increasing trend in interception efficiency with increasing wind speed for
328 the sparse and closed canopies (Figure 6b). A comparison of interception efficiencies binned for
329 low ($< 1 \text{ m s}^{-1}$) and high ($> 1 \text{ m s}^{-1}$) wind speeds by the Wilcoxon signed rank test, showed that
330 high wind speeds had significantly higher ($p < 0.05$) median interception efficiencies compared
331 to the low wind speed bins for the closed and sparse canopy. Conversely, the Wilcoxon test
332 showed the mixed canopy, which had an opening in the canopy towards the prevailing wind
333 direction (Figure 2b), had significantly higher ($p < 0.05$) median interception efficiencies for
334 the low wind speed bins.

335 Interception efficiency showed no association ($R^2 < 0.05$, $p > 0.2$) with the canopy load mea-
336 sured at the beginning of the 15-minute intervals (Table 4). The binned data show a small
337 increase in interception efficiency for all three canopies when the snow load is less than 7 mm
338 (Figure 6c). Interception efficiency later declined for snow loads greater than 7 mm for all
339 canopies, though this was inconsistent for the mixed canopy. A significantly greater ($p < 0.05$)
340 median interception efficiency was found for canopy snow loads less than 10 mm than those
341 with high initial canopy snow loads ($> 10 \text{ mm}$) using the Wilcoxon rank-test. Additional
342 statistics from ordinary least squares regression test on the 15-minute interval measurements
343 are provided in Table 4.

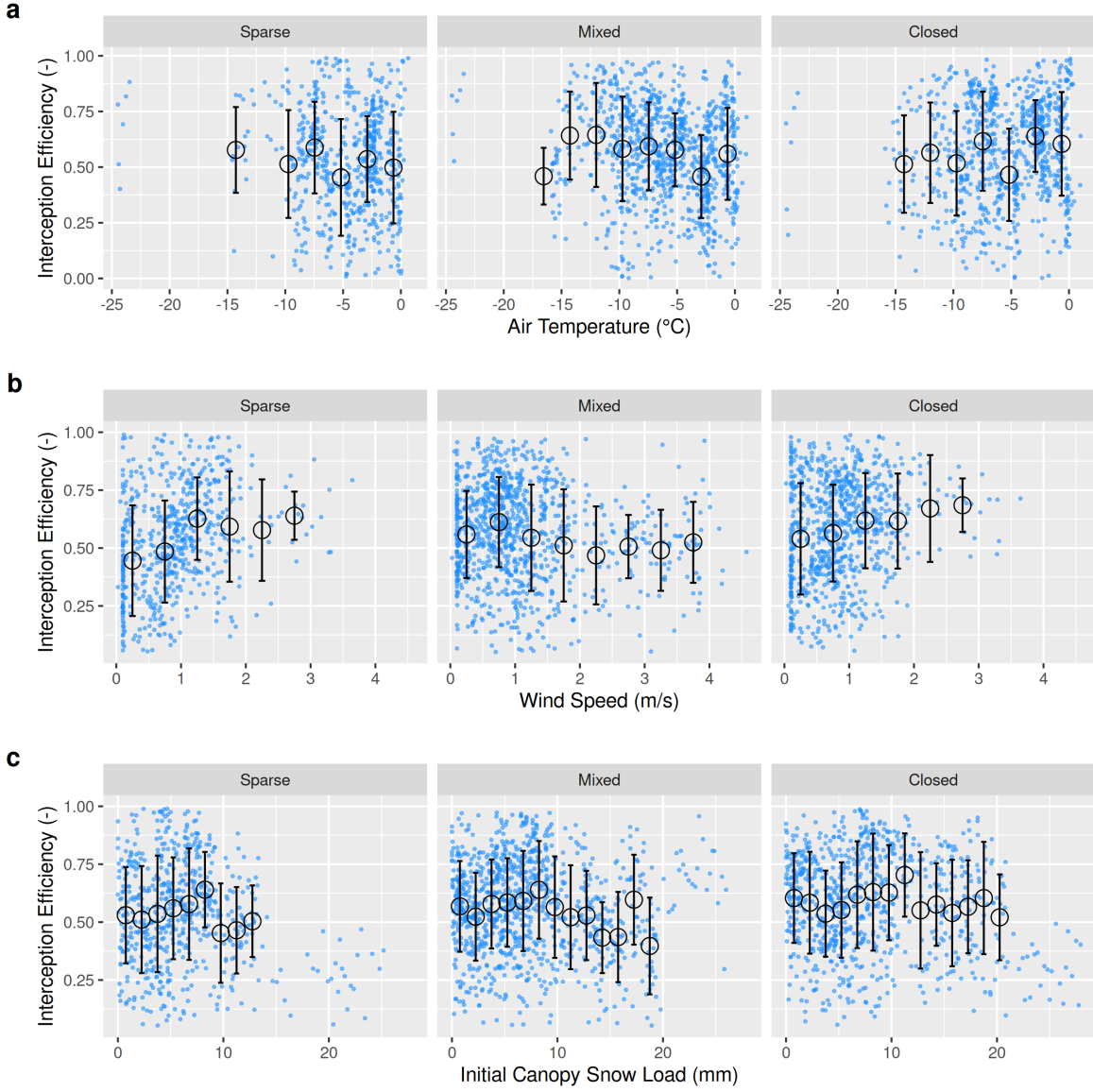


Figure 6: Scatter plots of 15-minute interval measurements (blue dots) and binned data (black open circles with error bars) of mean air temperature, mean wind speed, and initial canopy snow load versus mean snow interception efficiency. Panels show (a) air temperature, (b) wind speed, and (c) initial canopy snow load (the snow load observed at the beginning of the timestep). The black open circles show the mean of each bin and the error bars represent the standard deviations. See Table 4 for linear regression statistics.

Table 4: Statistics corresponding to the ordinary least squares linear regression test between 15-minute interval measurements of independent variables: mean air temperature, mean wind speed, and initial canopy snow load and the dependent variable mean interception efficiency. The test was run separately for three levels of canopy closure (C_l).

SCL					
Dependent Variable	Name	C_l	Adjusted R^2	p-value	n
Air Temperature (°C)	Mixed	0.75	0.026	0.000	1001
Air Temperature (°C)	Closed	0.79	0.011	0.002	830
Air Temperature (°C)	Sparse	0.64	0.011	0.006	609
Wind Speed (m/s)	Mixed	0.75	0.016	0.000	1001
Wind Speed (m/s)	Closed	0.79	0.026	0.000	830
Wind Speed (m/s)	Sparse	0.64	0.085	0.000	609
Initial Canopy Snow Load (mm)	Mixed	0.75	0.007	0.006	987
Initial Canopy Snow Load (mm)	Closed	0.79	0.012	0.001	815
Initial Canopy Snow Load (mm)	Sparse	0.64	0.038	0.000	598

4.2 The influence of forest structure on snow interception

UAV-lidar measurements of throughfall and canopy density provide insights on how the forest canopy influenced subcanopy snow accumulation during a wind-driven snowfall event between March 13th and 14th 2023. This event totaled 28.7 mm of snowfall at PWL station and was characterized by a transition from low rates of snowfall and air temperatures near 0°C to higher rates of snowfall by late afternoon on March 13th coinciding with air temperatures around -2.5 °C. An average wind speed of 1.3 m s⁻¹ and direction of 188° was observed 4.3 m above the ground at FT Station. Figure 7 shows the wind speed profile fit to the Prandtl-von Kármán log-linear relationship which differs from other wind speed profiles developed in dense canopy (e.g, Cionco, 1965). The predicted hydrometeor trajectory angles at varying heights, calculated using Equation 4 and the mean observed hydrometeor terminal velocity observed

over the event of 0.9 m s^{-1} are also shown in Figure 7. An average wind speed of 1.6 m s^{-1} and direction of 188° was calculated by integrating the wind speed from the surface to the mean canopy height of FT plot. The corresponding trajectory angle calculated using Equation 4 from this integrated wind speed was 61.5° .

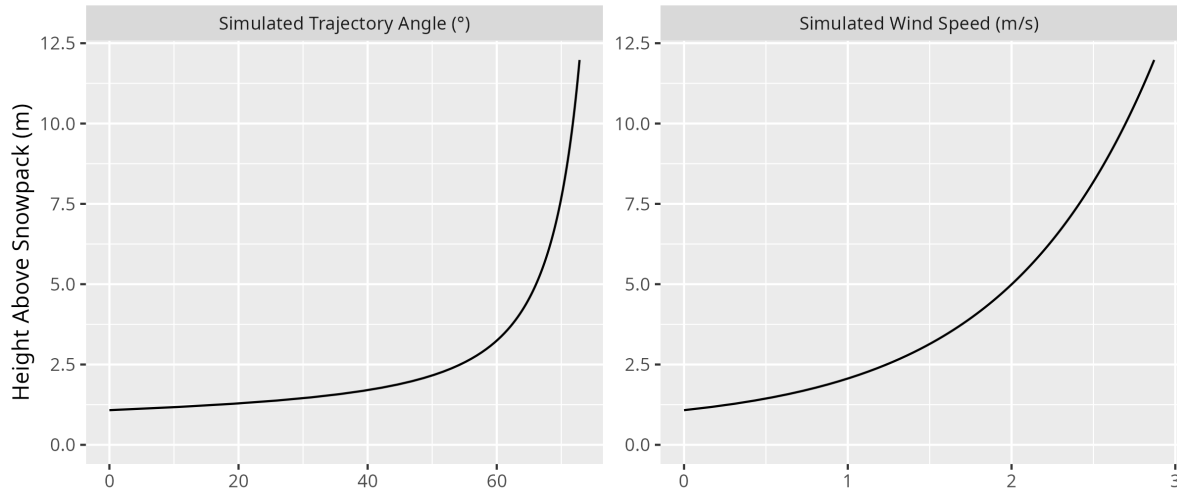


Figure 7: Wind speed profile using roughness length and displacement height parameters derived from anemometers at 2, 3, 4.3, and 13.5 m above ground at FT station over snow free periods and friction velocity estimated over the March 13–14th snowfall event.

Throughfall depth measured by UAV-lidar was close to the 28 in-situ manual measurements with a mean bias of -0.001 m and RMSE of 0.024 m. More details on the accuracy of UAV-lidar snowdepth measurements are provided in the supporting information section. Figure 8 shows the spatial distribution of throughfall and interception efficiency at the PWL and FT forest plots. Reduced throughfall and greater interception efficiency was observed on the north (lee) side of individual trees, which may be due to non-vertical hydrometeor trajectories caused by the steady southerly winds observed over this event. Transparent areas within the forest plots in Figure 8 represent grid cells that did not have any lidar ground returns (e.g., under dense canopy proximal to tree trunks) or were masked due to disturbance (e.g., walking paths in clearings). Visual observations on March 13th and 14th confirmed non-vertical hydrometeor

³⁶⁹ trajectories and increased canopy snow loads were observed on the windward side of individual
³⁷⁰ trees. This effect is shown in Figure 8 to be more apparent in the PWL forest plot than the
³⁷¹ FT forest plot. This may be attributed to the taller trees and higher canopy cover of the PWL
³⁷² forest plot compared to the FT forest plot, as for the same trajectory angle a taller tree will
³⁷³ produce a larger downwind footprint.

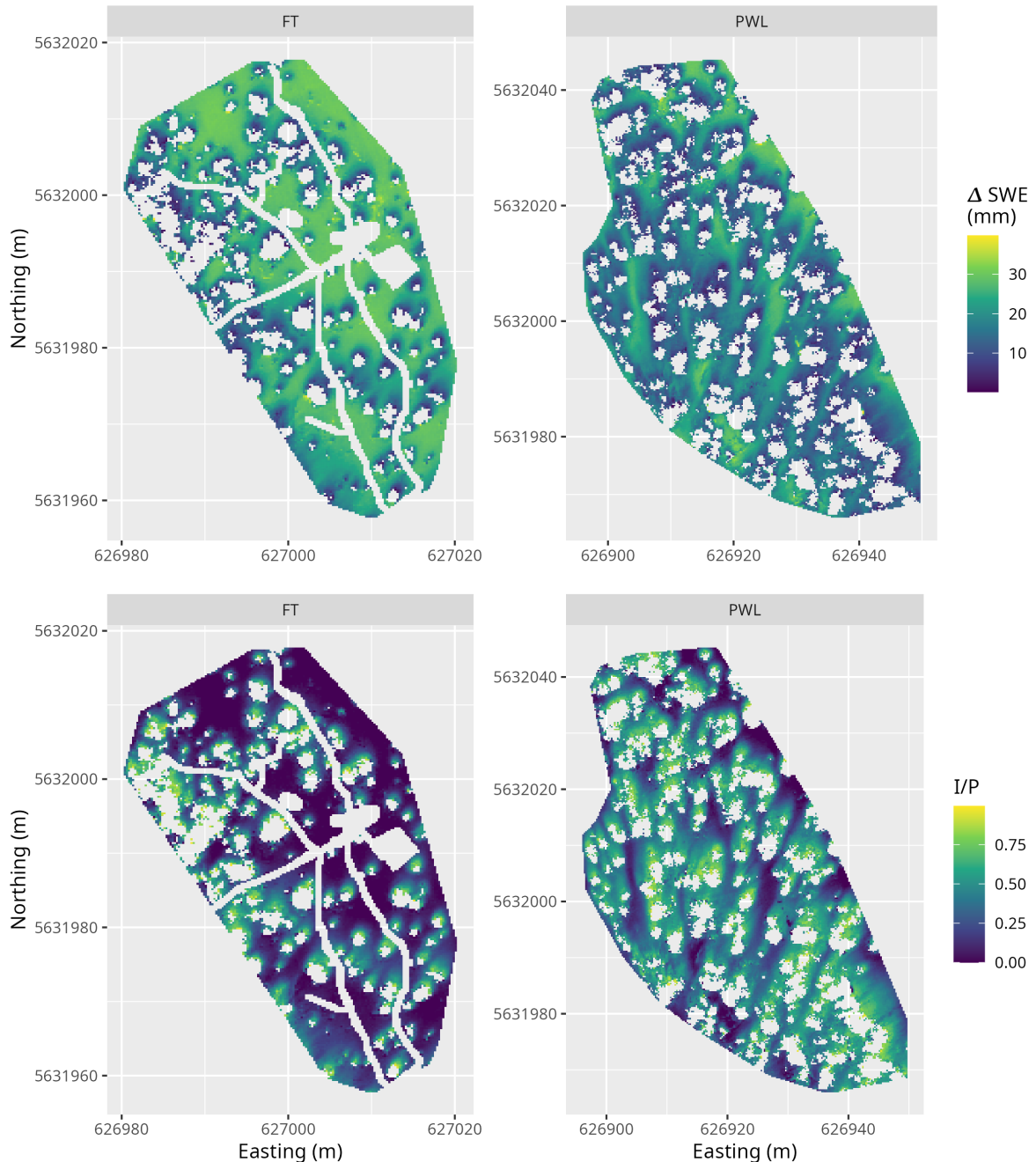


Figure 8: UAV-lidar measurements of the change in snow water equivalent, SWE (mm) and interception efficiency, I/P (-), over the March 13, 2023 24-hour snowfall event for the FT and PWL forest plots at a 0.25 m resolution. See the location of the two forest plots in Figure 1.

374 Figure 9 shows a strong linear correlation between C_p and interception efficiency towards
 375 the southern portion of the hemisphere, aligning with the average event wind direction. For
 376 the PWL forest plot, the upper 97.5th percentile of the ρ_p values shown in Figure 9, were
 377 found between azimuth angles of 167°–217°. Similarly, for the FT forest plot, the upper 97.5th
 378 percentile of ρ_p was found between azimuth angles of 171°–223°. The zenith angle found
 379 to have the highest correlation over this azimuth range was 22° ($\rho_p = 0.7$) and 21° ($\rho_p =$
 380 0.83) for PWL and FT respectively. The high correlation coefficients found for non-vertical
 381 zenith angles for both PWL and FT are hypothesized to result from non-vertical hydrometeor
 382 trajectories.

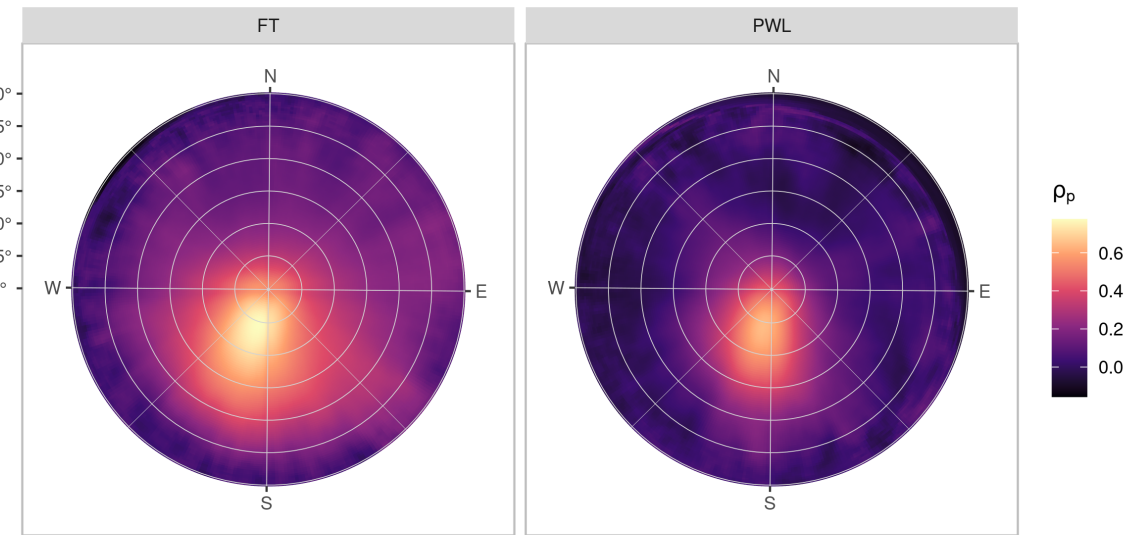


Figure 9: The Pearson Correlation Coefficient between rasters (0.25 m resolution) of interception efficiency and leaf contact area for each grid cell across the study site for each azimuth angles (0°, 1°, ..., 359°) and zenith angles (0°, 1°, ..., 90°) for the FT (left) and PWL (right) forest plots.

383 The correlation between C_p and interception efficiency, resampled to a 5 m grid resolution, was
 384 higher when C_p was adjusted for the observed shift in hydrometeor trajectory (Vector Based),
 385 compared to the leaf contact angle measured at a zenith angle of 0° (nadir) (Figure 10). The
 386 azimuth and zenith angles observed to have the highest ρ_p in Figure 9 was used to adjust

387 the vector based, C_p in Figure 10. The stronger association for the vector-based calculation
 388 suggests that adjusted C_p is a useful predictor of interception efficiency before ablation. An
 389 ordinary least squares linear regression forced through the origin was fit to the observed data
 390 points using the following equation:

$$\frac{I}{P} = C_p(C_c, \theta_h) \cdot \alpha \quad (9)$$

391 where α is an efficiency constant which determines the fraction of snowflakes that contact the
 392 C_p elements and are stored in the canopy (e.g., intercepted) before canopy snow unloading or
 393 ablation processes begin.

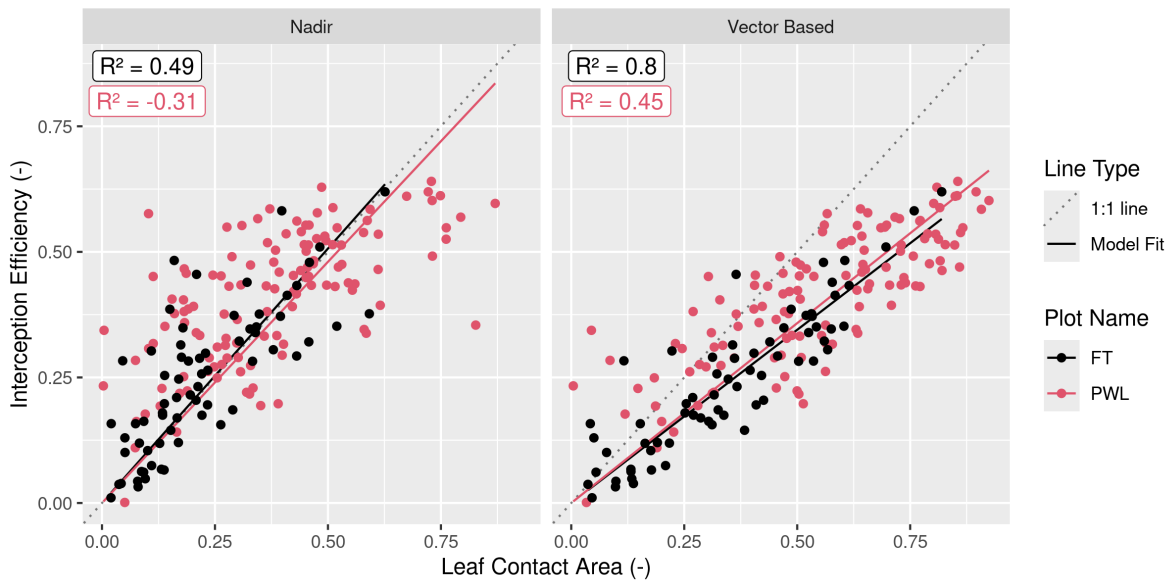


Figure 10: Scatter plots showing the relationship between leaf contact area and interception efficiency rasters resampled to a 5 m grid cell resolution. The left plot (nadir) shows leaf contact area measured from a zenith angle of 0°. The right plot (Vector Based) shows the leaf contact area averaged over rasters with zenith angles (PWL = 22°, FT = 21°) and azimuth angles (PWL = 167°, 178°, ... 217°; FT = 171°, 172°, ... 223°). The solid lines (Model fit) show an ordinary least squares linear regression forced through the origin and fitted to the PWL (red) and FT (black) data and the light grey dotted line shows a 1:1 line. The R^2 values for the four different models are shown in the upper right of each panel calculated following the methods outlined in Kozak & Kozak (1995).

394 For the vector-based model, the relationship between interception efficiency and C_p results in
395 R^2 values of 0.47 and 0.8 for PWL and FT respectively. The increase in interception efficiency
396 with C_p follows a reduced slope compared to the nadir models with α values of 0.71 and 0.68
397 for the PWL and FT vector-based models respectively. The reduced slope for the vector-based
398 models may be due to snowflakes that weaved through and/or bounced off branch elements
399 in addition to UAV-lidar measurement uncertainty which may have been slightly affected by
400 unloading and redistribution. These processes would have reduced the fraction of snowfall
401 that was stored in the canopy. Model error statistics are presented in Table 5 for the nadir
402 and vector-based models and show the vector-based model provided a better prediction of
403 interception efficiency. Some of the scatter observed in the nadir model shown in Figure 10
404 may be explained by grid cells which observed a greater interception efficiency compared to
405 the corresponding C_c value and can be attributed to the inability of C_c to represent the
406 increase in interception observed within canopy gaps in Figure 8. Conversely, grid cells where
407 interception efficiency is less than C_c , may be affected by non-vertical trajectory hydrometeors
408 making their way underneath the canopy as observed by the reduced interception efficiency
409 on the windward edges of individual trees in Figure 8. The latter explanation suggests the
410 non-linear relationship observed for the PWL nadir calculation in Figure 8.

Table 5: Model error statistics provided for predictions of interception efficiency using Equation 9 and for different a values, as shown in the Model Slope column. Statistics are provided for the PWL and FT forest plots, using leaf contact area canopy metrics adjusted to zenith angles of ($0^\circ, 1^\circ, \dots 30^\circ$) and azimuth angles ($170^\circ, 171^\circ, \dots 220^\circ$) and nadir zenith angle of 0° . The Mean bias is the difference in the model and observed values, MAE is the mean of the absolute error, RMS Error is the root mean squared error, R^2 is the coefficient of determination adjusted using Equation 10 in Kozak & Kozak (1995).

Plot	Canopy	Model Slope	Mean Bias	MAE	RMS Error	
Name	Calculation	(-)	(-)	(-)	(-)	R^2
FT	Nadir	0.99	0.022	0.071	0.099	0.51
FT	Vector Based	0.68	0.001	0.047	0.062	0.80
PWL	Nadir	0.95	0.048	0.113	0.146	NA
PWL	Vector Based	0.71	0.019	0.078	0.095	0.47

411 **4.3 The combined influence of trajectory angle and forest structure on
412 interception**

413 Figure 11 shows that C_p , measured from VoxRS prior to snowfall on March 13th, increases
414 substantially with simulated hydrometeor trajectory angle and corresponding simulated wind
415 speed. The standard deviation in VoxRS measured C_p , illustrated by the shaded area in
416 Figure 11, exhibits the broad range in values for individual grid cells across each forest plot.
417 Despite this large scatter, a systematic increase in the mean C_p across both forest plots results
418 from a rise in the number of canopy elements for more horizontal angles, when averaged across
419 each forest plot, over all azimuth angles (see top left panel Figure 11). This results in a large
420 rise in C_p over relatively common estimated wind speeds. For example, with a wind speed
421 of 1 m s^{-1} and estimated trajectory angle of 48° , C_p would increase by 0.31 and 0.28 for the
422 PWL and FT forest plots respectively (Figure 11). This is a fractional increase in the plot C_p
423 from nadir of 0.61 and 0.95 for PWL and FT respectively. The increase in C_p from C_c , with
424 increasing trajectory angle is shown on the bottom row of Figure 11 and exhibits a similar

⁴²⁵ relationship for both forest plots FT and PWL until trajectory angles reach approximately
⁴²⁶ 60°. Beyond 60°, the PWL rate of increase slows as the C_p approaches 1.0, while the FT plot,
⁴²⁷ which has lower C_c , continues to rise until around 75° as a C_p of 1.0 is approached. C_p was
⁴²⁸ also quantified across trajectory angles for both PWL and FT on March 14th, post snowfall,
⁴²⁹ and showed a negligible increase in C_p compared to C_p measured on March 13th without snow
⁴³⁰ in the canopy.

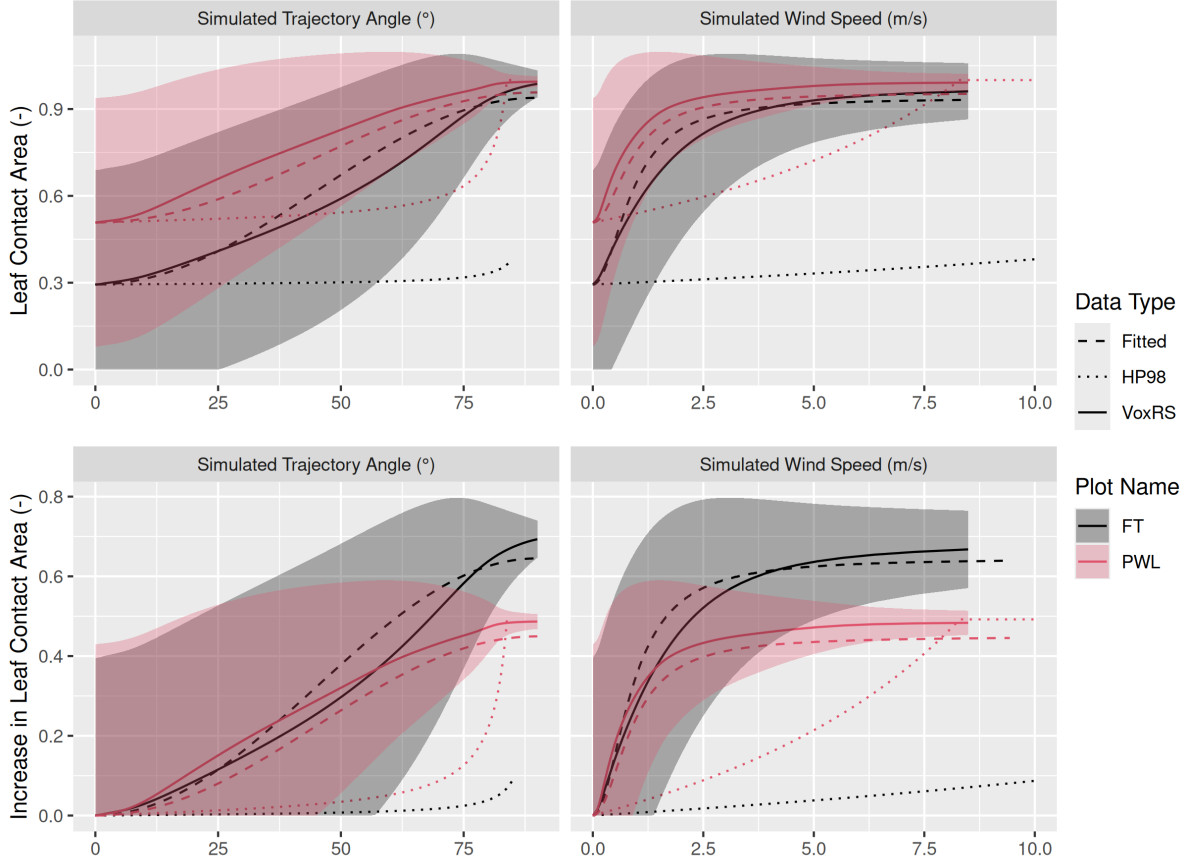


Figure 11: Plots showing the relationship between hydrometeor trajectory angle (left column) and wind speed (right column) with mean plot-wide snow-leaf contact area, C_p (top row) and the increase in mean plot-wide C_p , e.g., $C_p - C_c$ (bottom row). The simulated hydrometeor trajectory angle is measured as degrees from zenith. Simulated wind speed was calculated as a function of hydrometeor trajectory angle by rearranging Equation 4 and an observed event hydrometeor fall velocity of 0.9 m s^{-1} . The solid lines (VoxRS) represent the mean C_p (top row) or increase in mean C_p (bottom row) for a single zenith angle observed from VoxRS across all grid cells for each forest plot and across all azimuth angles. The shaded area represents 1 standard deviation above and below the observed VoxRS mean. The dashed lines (Fitted) represent predictions from Equation 10 (top row) and Equation 11 (bottom row). The dotted lines (HP98) represent the predictions from Equation 10 in Hedstrom & Pomeroy (1998). A forested downwind distance of 100 m was assumed for the HP98 calculation.

⁴³¹ A function is proposed here to calculate plot-scale leaf contact area, C_p (-):

$$C_p = C_c + C_{inc}(\theta_h, C_c) \quad (10)$$

432 where, C_{inc} represents the increase in leaf contact area from C_c , and it is a function of θ_h .
 433 To estimate C_{inc} in the absence of detailed canopy measurements, the following function is
 434 proposed:

$$C_{inc} = (1 - C_c) \cdot f(\theta_h) \quad (11)$$

435 where $1 - C_C$ represents the void space in the canopy, and $f(\theta_h)$ is a function describes the
 436 relative increase in canopy area as a function of θ_h . Here, $f(\theta_h)$ is approximated here as:

$$f(\theta_h) = b \cdot \sin(\theta_h)^2 \quad (12)$$

437 where b is a fitting coefficient, estimated to be ~0.91 through a non-linear least squares regres-
 438 sion fit to the VoxRS measurements at both FT and PWL. The use of $\sin(\theta_h)^2$ in Equation 12
 439 reflects the relative increase in snow-leaf contact area, which also leads to a proportional
 440 decrease in the canopy void space ($1 - C_c$). The assumptions of Equation 12 include its appli-
 441 cation to a forest with relatively uniform structure (e.g., without large clear cuts) and where
 442 the mean height of the canopy is greater than the mean width of individual trees.

443 Simulated C_p using Equation 10 is shown in the dashed lines in the top row of Figure 11
 444 and follows the VoxRS-measured mean C_p closely. Model error statistics shown in Table 6
 445 demonstrate that Equation 11 performed well, with a mean bias and RMSE of (-) and (-)
 446 respectively for PWL, and (-) and (-) for FT. In contrast, Table 6 reveals that the Hedstrom
 447 & Pomeroy (1998) method produced significantly less accurate estimates of C_p , with a mean
 448 bias and RMSE of -0.2 (-) and 0.23 (-) respectively for PWL, and -0.26 (-) and 0.32 (-) for
 449 FT.

Table 6: Model error statistics calculated for the prediction of leaf contact area from trajectory angle using Equation 11 (Eq. 11) and Equation 10 from Hedstrom & Pomeroy (1998) for the PWL and FT forest plots. Mean bias is the difference in the model and observed values, MAE is the mean of the absolute error, RMS Error is the root mean squared error and R^2 is the coefficient of determination. The units for all metrics are dimensionless. A forested downwind distance of 100 m was used for the HP98 calculation.

Model	Plot Name	Mean Bias (-)	MAE (-)	RMS Error (-)	R^2
HP98	FT	-0.26	0.26	0.32	-0.97
HP98	PWL	-0.20	0.20	0.23	-0.96
Eq. 10	FT	0.03	0.04	0.05	0.95
Eq. 10	PWL	-0.05	0.05	0.05	0.90

450 4.4 Throughfall model performance

451 The performance of Equations 9, 10, and 11 in estimating event throughfall was assessed
 452 against UAV-lidar measurements of throughfall for the March 13–14th snowfall event at the
 453 plot scale for both FT and PWL. Required values for the model included the event mean
 454 hydrometeor terminal velocity and event total snowfall which were measured at PWL station,
 455 and wind speed was taken as one-third the mean canopy height using the wind speed profile in
 456 Figure 7. Additional model inputs include the mean C_c for each plot which was measured from
 457 the VoxRS dataset. An α value of 0.874 (-) was found through calibration which provided the
 458 best fit between observed and simulated interception efficiency at the plot scale for both FT
 459 and PWL.

460 Figure 12 shows the vector-based model, computed using Equation 9 with C_p adjusted for
 461 estimated hydrometeor trajectory angle, closely matches UAV-lidar measurements of through-
 462 fall. Observed and modelled values of interception efficiency and ΔSWE_{tf} are presented in
 463 Table 7 along with corresponding error statistics. Modelled throughfall from the vector-based
 464 model was 17.5 mm compared to the measured throughfall of 16.6 mm for PWL. For FT, the

465 vector-based modelled throughfall was 21.3 mm, while the measured values were 22.1 mm.
 466 The vector-based model shows a lower mean bias of -0.8 mm for PWL and a negative bias of
 467 0.8 mm for FT, compared to the larger mean bias of -1.6 mm for PWL and -0.8 mm for FT
 468 with the nadir-model (calculated using C_c in place of C_p). This resulted in a large reduction in
 469 the percent error in predicted throughfall, from -9.4% with the nadir-model to -1.8% with the
 470 vector-based model for PWL. A smaller improvement was observed for FT, with the percent
 471 error in predicted throughfall declining from -3.6% with the nadir-model to -1.4% with the
 472 vector-based model.

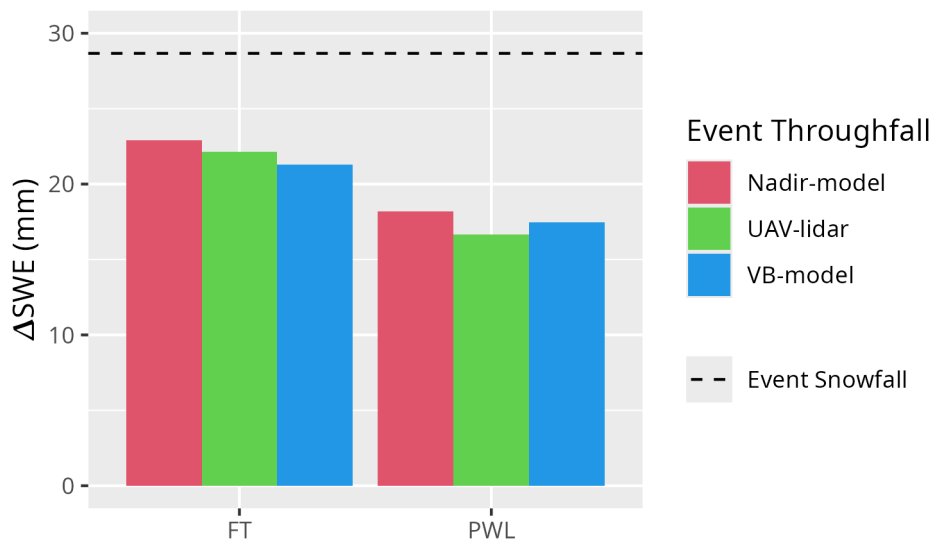


Figure 12: Bar chart comparing the observed and modelled mean change in throughfall (ΔSWE , mm) over the March 13-14 snowfall event averaged over forest plots FT and PWL. The ‘Nadir-model’ used Equation 9 not adjusted for trajectory angle (e.g., C_c) and the Vector-based ‘VB-model’ which uses Equation 9 with C_p adjusted for trajectory angle. ‘UAV-lidar’ corresponds to throughfall calculated using Equation 6 incorporating UAV-lidar snow depth and snow density from in-situ snow pits. The black horizontal dashed line shows the accumulated SWE (mm) over the snowfall event to the PWL station open clearing.

Table 7: Model error statistics for model estimates of snow interception efficiency (I/P) and throughfall (TF) compared to measurements of I/P and TF using UAV-lidar averaged over the FT and PWL forest plots. Units for I/P are (-) and TF are (mm). The vector-based model utilized Equation 9 with C_p adjusted for trajectory angle. The nadir model also utilized Equation 9 but was not adjusted for trajectory angle and thus C_c was used instead of C_p . The ‘Obs. Value’ column contains measurements from UAV-lidar while the ‘Mod. Value’ column contains the modelled values. The mean bias was calculated as observed minus modelled and percent error is the percent error between predicted and observed values.

	Model	Value		Obs.	Mod.	Mean	
Plot	Type	Name	Units	Value	Value	Bias	Perc. Error
FT	VB-model	I/P	-	0.23	0.26	-0.03	-12.74
FT	Nadir-model	I/P	-	0.23	0.20	0.03	12.10
FT	VB-model	TF	mm	22.12	21.29	0.83	3.77
FT	Nadir-model	TF	mm	22.12	22.91	-0.79	-3.58
PWL	VB-model	I/P	-	0.42	0.39	0.03	6.94
PWL	Nadir-model	I/P	-	0.42	0.37	0.05	12.95
PWL	VB-model	TF	mm	16.64	17.48	-0.83	-5.01
PWL	Nadir-model	TF	mm	16.64	18.20	-1.56	-9.35

⁴⁷³ **5 Discussion**

⁴⁷⁴ **5.1 Influence of Air Temperature, Wind Speed and Canopy Snow Load on Initial
475 Interception**

⁴⁷⁶ The point scale observations presented in Figure 6 show air temperature had little influence
⁴⁷⁷ on initial interception efficiency. This finding aligns with Storck et al. (2002), who observed
⁴⁷⁸ that variations in air temperature and wind speed did not significantly affect snow interception
⁴⁷⁹ by mature canopies under the meteorological conditions studied. Air temperature influences
⁴⁸⁰ processes that both increase or decrease interception efficiency, which may occur simultaneously
⁴⁸¹ and limit the overall effect. For example, warmer temperatures increase branch flexibility
⁴⁸² (Schmidt & Gluns, 1991), and can cause snow loaded branches to bend and thus reduce C_p .
⁴⁸³ In contrast, the cohesion and adhesion of snowfall has been shown to increase for warmer
⁴⁸⁴ temperatures (Kobayashi, 1987; Pfister & Schneebeli, 1999) which could increase the efficiency
⁴⁸⁵ constant, α in Equation 9 thus increasing interception efficiency.

⁴⁸⁶ A weak relationship, that leaves 80–90% of variance unexplained, was observed between initial
⁴⁸⁷ interception efficiency (before unloading) with increasing wind speed at two locations which
⁴⁸⁸ were sheltered from the predominant wind direction (Figure 6b). This is attributed to an
⁴⁸⁹ associated increase in C_p due to non-vertical hydrometeor trajectories. These results are
⁴⁹⁰ consistent with observations by Schmidt & Troendle (1989) who observed a slight increase
⁴⁹¹ in snowfall interception with increasing wind speeds up to 6 m s^{-1} and studies of rainfall
⁴⁹² interception by Herwitz & Slye (1995) and Van Stan et al. (2011).

⁴⁹³ Compared to the influence of wind speed, interception efficiency showed a smaller sensitivity
⁴⁹⁴ to canopy snow load at the point scale (Figure 5). The slight increase in interception efficiency
⁴⁹⁵ for smaller canopy snow loads and decline for larger canopy snow loads is attributed to the
⁴⁹⁶ influence of canopy snow load on C_p (Figure 6c). While small, this effect is consistent with
⁴⁹⁷ the theory proposed by Satterlund & Haupt (1967) that interception efficiency increases as
⁴⁹⁸ the canopy fills with snow bridging gaps in the canopy, while later declining due to branch

499 bending and decreased canopy cover. However, at the plot-scale Staines & Pomeroy (2023),
500 show that these two processes may partially compensate for each other as C_p increases in
501 closed canopy as new snow covers gaps in the canopy but decreases in partially open canopy
502 due to branch bending. The increase in C_p resulting from snow load in Staines & Pomeroy
503 (2023) was small compared to the substantial rise in C_p due to trajectory angle presented in
504 their study. Which corroborates with the plot-scale observations of C_p in this study shown
505 in Figure 11. Moreover, additional studies (Calder, 1990; Watanabe & Ozeki, 1964) align
506 with the observations in Figure 6 and Figure 3, suggest little evidence of reduced interception
507 efficiency with increasing canopy snow load. Further evidence in support of the relatively small
508 influence of canopy snow load on C_p , is provided by Lundquist et al. (2021) who reported
509 improved simulation of subcanopy snow accumulation without the use of a maximum canopy
510 snow load, when linked with a comprehensive canopy snow ablation routine. Lehtonen et
511 al. (2016) also note that in northern Finland heavy canopy snow loads have been observed
512 to continue increasing until stem breakage, under conditions favourable for the formation of
513 significant rime-ice accretion and limited ablation, thus reducing C_p . Models are available to
514 predict the accretion of ice on tree canopies (e.g., Nock et al., 2016) however, further research is
515 required to understand the canopy snow load required to cause stem breakage across different
516 tree species and canopy loads. The low sensitivity of interception efficiency with canopy snow
517 load found in this study and others may be attributed to several factors: a reduced inclusion
518 of ablation processes in the interception efficiency measurements, limited influence of canopy
519 snow load on C_p at this study site, and/or the compensatory effects outlined by Satterlund &
520 Haupt (1967).

521 **5.2 The Influence of Canopy Snow Ablation on Previous Theories**

522 These findings on the limited influence of air temperature and canopy snow load on initial in-
523 terception differ from the theories underpinning existing snow interception parameterizations
524 (Hedstrom & Pomeroy, 1998; Moeser et al., 2015; Satterlund & Haupt, 1967; Storck et al.,
525 2002). Cebulski & Pomeroy (2025) highlights the uncertainty in the extent to which ablative

processes are included in common snow interception models. Since canopy snow ablation is strongly related to air temperature and snow load (Ellis et al., 2010; Floyd, 2012; Hedstrom & Pomeroy, 1998; Roesch et al., 2001) some the previously observed relationships related to these variables may be explained by changes in ablation rather than initial interception. Moreover, since a canopy snow load capacity was not observed in this study, the air temperature dependent canopy snow load capacities included in the Hedstrom & Pomeroy (1998) and Andreidis et al. (2009) models were not applicable. Studies that have identified a relationship between air temperature and interception efficiency (Katsushima et al., 2023; Roth & Nolin, 2019), were not explicitly focused on initial interception, prior to canopy snow ablation, and therefore likely include substantial ablation processes in their measurements. Consequently, the relationships in Roth & Nolin (2019) Katsushima et al. (2023) may be more strongly influenced by the effects of air temperature on canopy snow ablation. The coupling of ablation processes within existing snow interception models may contribute to overestimates of throughfall, canopy snow unloading, and canopy snow melt when combined with other canopy snow ablation parameterizations (Cebulski & Pomeroy, 2025).

5.3 Justification and Limitations of a New Snow Interception Model

To address these issues, a new vector-based snow interception parameterization, Equation 9, is presented which calculates initial interception efficiency as a function of C_p and α . This new parameterization allows for canopy snow loading processes to be isolated from canopy snow ablation processes and is consistent with current rainfall interception theory (Valante et al., 1997). Equation 9 differs only slightly from the original Hedstrom & Pomeroy (1998) parameterization (see Equation 6 in Hedstrom & Pomeroy 1998), in that it does not calculate interception efficiency as a function of canopy snow load and from the Storck et al. (2002) parameterization who found interception efficiency to be constant. The theoretical basis of the α parameter in Equation 9 is that the association between C_p and interception efficiency, as shown in Figure 10, unlike existing rainfall parameterizations (Valante et al., 1997) does not follow a 1:1 line, as falling snow hydrometeors may bounce off the canopy elements. Further

research is needed to explore how processes such as the increased cohesion and adhesion of snowfall to the canopy at warm temperatures, as observed by Kobayashi (1987), Pfister & Schneebeli (1999), as well as hydrometeor velocity, particle size, and shape suggested by (Katsushima et al., 2023), may influence the α parameter, although these effects were not observed in this study. Moreover, the relationship between C_p and air temperature, canopy snow load, and canopy structure is expected to vary across varying combinations of climate, forest species and ages, requiring further research. For example, certain tree species or younger trees with very flexible branches may warrant the explicit representation of variable C_p with canopy snow load. Since Equation 9 intentionally excludes processes attributed to canopy snow ablation that were previously included in earlier snow interception models, these ablation processes must be incorporated in canopy snow ablation parameterizations to fully represent the canopy snow mass balance.

Measurements of interception efficiency, as shown in Figure 8, align with the theory proposed by Hedstrom & Pomeroy (1998) which suggests reduced throughfall on the lee side of individual trees for a wind driven snowfall event. However, an existing exponential relationship proposed in Hedstrom & Pomeroy (1998) to scale C_p with wind speed failed to reproduce the observations presented in Figure 11. Instead, plot-wide C_{inc} was found to increase as function of θ_h and C_c . Significant scatter in VoxRS measured C_p across the two forest plots, illustrated by the high standard deviation in Figure 11, resulted from variability in canopy density across different locations and azimuth angles. This large scatter suggests the observed relationships in Figure 11 are only applicable at the forest stand scale where the sub-metre variability in C_p averages out. For example, at the point scale, the mixed canopy SCL which is open to the prevailing wind direction (Figure 2), had an increase in throughfall with increasing wind speed (Figure 5 & Figure 6). However, Figure 11 shows that at the plot scale, C_p rises with increasing θ_h , as there is a greater number of grid cells which have more closed canopy at more horizontal angles. Still, Equation 11 would not be applicable in areas that have large continuous gap fractions (e.g., large forested clear cuts) that are many times wider than the mean canopy height. Further testing of Equation 11 is also needed in a wide range of forest species, ages,

581 densities, and structures. Staines & Pomeroy (2023) have also shown that backflows and large
582 eddies that occur within the canopy can also contribute to mixed responses.

583 It was found that the mean event hydrometeor trajectory angle, required for Equation 11, could
584 be predicted from Equation 4 using the observed mean hydrometeor fall velocity and the mean
585 horizontal wind speed selected at one-third of the canopy height above the ground. A wind
586 speed at one-third the mean canopy height is hypothesized to be important for canopy snow
587 accumulation as a large fraction of the horizontal cross-sectional area is at this height for most
588 needleleaf canopies. Katsushima et al. (2023), also proposed the wind speed at one-third the
589 canopy height for modelling unloading of canopy snow as it corresponds to the centre of gravity
590 when the horizontal projection of the canopy is assumed to be a triangle. However, there is
591 uncertainty in the transferability of the canopy height observed here to other environments
592 due to differing tree structures and tree species. This may include forests with a larger trunk
593 space or have more of their canopy contact area at higher heights above the ground (e.g., some
594 deciduous canopies). Moreover, Equation 4 assumes a linear hydrometeor trajectory, and does
595 not consider non-linear patterns such as wind flow directions around tree elements, turbulent
596 flow, or differences in wind speed with height.

597 Although the improvement in performance of the vector-based model over the nadir model was
598 relatively small, the vector-based model is preferred due to its overall lower error compared
599 to the UAV-lidar measurements and better representation of physical processes. While the
600 vector-based model acts to increase interception efficiency with wind speed, several studies
601 have shown that canopy snow ablation increases as a result of wind induced unloading (Bartlett
602 & Verseghy, 2015; Betts & Ball, 1997; Lumbrazo et al., 2022; Roesch et al., 2001; Wheeler,
603 1987). Thus, representing both the increase in initial interception due to inclined hydrometeor
604 trajectory angles and the subsequent increase in canopy snow unloading will be important
605 in subcanopy snow accumulation models. This new vector-based model has been developed
606 and tested based at the forest plot scale (\sim 100s of m^2) and is therefore currently suitable
607 for application in hydrological models at this scale that discretize by forest density. Previous
608 models were developed based on process understanding at varying scales: Hedstrom & Pomeroy

609 (1998), based on snow survey transects at the forest plot scale (intervals ranging from days to
610 weeks), and Storck et al. (2002), based on point-scale 30-minute interval lysimetry observations.
611 Recent evidence from Staines & Pomeroy (2023) and the results presented here suggest that
612 some of the process understanding developed in previous studies may not be applicable at
613 larger scales or finer spatial and temporal resolutions. Therefore, the process understanding
614 presented here may be more suitable for application at larger extents and finer temporal
615 resolutions, however, further testing is required to support this theory.

616 **6 Conclusions**

617 New observations of initial snow interception, collected over a wide range of meteorological
618 conditions and canopy densities indicate that forest is the primary factor influencing subcanopy
619 snow accumulation. At the point scale, high-temporal resolution measurements revealed no
620 evidence of a maximum canopy snow load, even for event snowfalls up to 45 mm, nor was
621 there any indication of air temperature influencing the cohesion and adhesion of snowfall to
622 the canopy or branch bending reducing canopy cover. Instead, wind speed was found to
623 influence interception efficiency by changing the hydrometeor trajectory angle, which can lead
624 to a substantial increase in snow-leaf contact area.

625 At the forest plot scale, UAV-lidar measurements of throughfall aligned with the point-scale
626 observations demonstrating that leaf contact area was the primary factor influencing inter-
627 ception efficiency at a particular site. Leaf contact area, which incorporates changes in the
628 number of canopy contacts with hydrometeor trajectory angle, proved to be a better predictor
629 of interception efficiency compared to nadir-calculated canopy cover. When averaged across
630 each forest plot, leaf contact area was shown to be highly sensitive to trajectory angle, in-
631 creasing by 61–95% for trajectory angles associated with a 1 m s^{-1} wind speed. An existing
632 theoretical relationship failed to adequately represent the VoxRS-measured increase in leaf
633 contact area with simulated trajectory angles. As a result, a new relationship is proposed as a

634 function of canopy cover and hydrometeor trajectory angle (approximated from wind speed),
635 which demonstrated good performance at this study site.

636 The weak association between air temperature and canopy snow load with interception effi-
637 ciency, as presented here and in other recent studies, coupled with the influence of wind speed
638 on leaf contact area, highlights the need for a new snow interception parameterization. A new
639 parameterization is proposed that calculates initial interception as a function of snowfall and
640 leaf contact area. This parameterization is consistent with rainfall interception studies, which
641 also separate canopy loading and ablation processes, and calculate interception as a function
642 of canopy cover. Additionally, a second equation is proposed to estimate leaf contact area
643 as a function of hydrometeor trajectory angle and nadir canopy cover. This updated snow
644 interception parameterization performed well in the subalpine forest studied here at the forest
645 plot scale. However, further validation is necessary in a range of climates, forests, and larger
646 spatial extents.

647 **7 Acknowledgments**

648 We wish to acknowledge financial support from the University of Saskatchewan Dean's Schol-
649 arship, Natural Sciences and Engineering Research Council of Canada, Global Water Futures
650 Programme, Environment and Climate Change Canada, Alberta Innovates, Canada Founda-
651 tion for Innovation, and the Canada Research Chairs Programme. We thank Madison Harasyn,
652 Hannah Koslowsky, Kieran Lehan, Lindsey Langs and Fortress Mountain Resort for their help
653 in the field. Jacob Staines, Madison Harasyn, Alistair Wallace, and Rob White contributed
654 to developing the UAV-lidar processing workflow.

655 **8 Data Availability**

656 The data that support the findings in this study are available at <https://doi.org/10.5281/zenodo.14018893>.

657 **References**

- 658 Andreadis, K. M., Storck, P., & Lettenmaier, D. P. (2009). Modeling snow accumulation
659 and ablation processes in forested environments. *Water Resources Research*, 45(5), 1–33.
660 <https://doi.org/10.1029/2008WR007042>
- 661 Bartlett, P. A., & Verseghy, D. L. (2015). Modified treatment of intercepted snow improves
662 the simulated forest albedo in the Canadian Land Surface Scheme. *Hydrological Processes*,
663 29(14), 3208–3226. <https://doi.org/10.1002/HYP.10431>
- 664 Betts, A. K., & Ball, J. H. (1997). Albedo over the boreal forest. *Journal of Geophysical
665 Research: Atmospheres*, 102(D24), 28901–28909. <https://doi.org/10.1029/96JD03876>
- 666 Calder, I. R. (1990). *Evaporation in the uplands* (p. 148). Wiley.
- 667 Cebulski, A. C., & Pomeroy, J. W. (2025). Theoretical Underpinnings of Snow Interception
668 and Canopy Snow Ablation Parameterisations. *WIREs Water*, 12(e70010). [https://doi.or
g/10.1002/wat2.70010](https://doi.or
669 g/10.1002/wat2.70010)
- 670 Chianucci, F., & Macek, M. (2023). hemispheR: An R package for fisheye canopy image
671 analysis. *Agricultural and Forest Meteorology*.
- 672 Cionco, R. M. (1965). A mathematical model for air flow in a vegetative canopy. *Journal of
673 Applied Meteorology (1962)*, 4(4), 517–522. [https://doi.org/10.1175/1520-0450\(1965\)004
%3C0517:AMMFAF%3E2.0.CO;2](https://doi.org/10.1175/1520-0450(1965)004
674 %3C0517:AMMFAF%3E2.0.CO;2)
- 675 Ellis, C. R., Pomeroy, J. W., Brown, T., & MacDonald, J. (2010). Simulation of snow accumu
676 lation and melt in needleleaf forest environments. *Hydrology and Earth System Sciences*,
677 14(6), 925–940. <https://doi.org/10.5194/hess-14-925-2010>
- 678 Ellis, C. R., Pomeroy, J. W., & Link, T. E. (2013). Modeling increases in snowmelt yield and
679 desynchronization resulting from forest gap-thinning treatments in a northern mountain
680 headwater basin. *Water Resources Research*, 49(2), 936–949. [https://doi.org/10.1002/wr
cr.20089](https://doi.org/10.1002/wr
681 cr.20089)
- 682 Essery, R., Pomeroy, J. W., Parviainen, J., & Storck, P. (2003). Sublimation of snow from
683 coniferous forests in a climate model. *Journal of Climate*, 16(11), 1855–1864. [https://doi.org/10.1175/1520-0442\(2003\)016%3C1855:SOSFCF%3E2.0.CO;2](https:
684 //doi.org/10.1175/1520-0442(2003)016%3C1855:SOSFCF%3E2.0.CO;2)

- 685 Floyd, W. C. (2012). *Snowmelt energy flux recovery during rain-on-snow in regenerating forests*
686 (p. 180) [PhD thesis, University of British Columbia]. <https://doi.org/https://dx.doi.org/10.14288/1.0073024>
- 688 Fryer, B. Y. G. I., Johnson, E. A., Fryer, G. I., & Johnson, E. A. (1988). Reconstructing
689 fire behaviour and effects in a subalpine forest. *The Journal of Applied Ecology*, 25(3),
690 1063–1072. <https://doi.org/10.2307/2403766>
- 691 Gelfan, A. N., Pomeroy, J. W., & Kuchment, L. S. (2004). Modeling forest cover influences on
692 snow accumulation, sublimation, and melt. *Journal of Hydrometeorology*, 5(5), 785–803.
693 [https://doi.org/10.1175/1525-7541\(2004\)005%3C0785:MFCIOS%3E2.0.CO;2](https://doi.org/10.1175/1525-7541(2004)005%3C0785:MFCIOS%3E2.0.CO;2)
- 694 Golding, D. L., & Swanson, R. H. (1978). Snow accumulation and melt in small forest openings
695 in Alberta. *Canadian Journal of Forest Research*, 8(4), 380–388. <https://doi.org/10.1139/x78-057>
- 697 Harder, P., & Pomeroy, J. W. (2013). Estimating precipitation phase using a psychrometric
698 energy balance method. *Hydrological Processes*, 27(13), 1901–1914. <https://doi.org/10.1002/hyp.9799>
- 700 Harder, P., Pomeroy, J. W., & Helgason, W. D. (2020). Improving sub-canopy snow depth
701 mapping with unmanned aerial vehicles: Lidar versus structure-from-motion techniques.
702 *The Cryosphere*, 14(6), 1919–1935. <https://doi.org/10.5194/tc-14-1919-2020>
- 703 Harpold, A. A., Krogh, S. A., Kohler, M., Eckberg, D., Greenberg, J., Sterle, G., & Broxton,
704 P. D. (2020). Increasing the efficacy of forest thinning for snow using high-resolution
705 modeling: A proof of concept in the Lake Tahoe Basin, California, USA. *Ecohydrology :
706 Ecosystems, Land and Water Process Interactions, Ecohydrogeomorphology*, 13(4). <https://doi.org/10.1002/eco.2203>
- 708 Hedstrom, N. R., & Pomeroy, J. W. (1998). Measurements and modelling of snow interception
709 in the boreal forest. *Hydrological Processes*, 12(10-11), 1611–1625. [https://doi.org/10.1002/\(SICI\)1099-1085\(199808/09\)12:10/11%3C1611::AID-HYP684%3E3.0.CO;2-4](https://doi.org/10.1002/(SICI)1099-1085(199808/09)12:10/11%3C1611::AID-HYP684%3E3.0.CO;2-4)
- 711 Herwitz, S. R., & Slye, R. E. (1995). Three-dimensional modeling of canopy tree interception
712 of wind-driven rainfall. *Journal of Hydrology*, 168(1-4), 205–226. [https://doi.org/10.1016/0022-1694\(94\)02643-P](https://doi.org/10.1016/0022-1694(94)02643-P)

- 714 Isyumov, N. (1971). *An approach to the prediction of snow loads* [PhD thesis]. The University
715 of Western Ontario (Canada).
- 716 Katsushima, T., Kato, A., Aiura, H., Nanko, K., Suzuki, S., Takeuchi, Y., & Murakami, S.
717 (2023). Modelling of snow interception on a Japanese cedar canopy based on weighing
718 tree experiment in a warm winter region. *Hydrological Processes*, 37(6), 1–16. <https://doi.org/10.1002/hyp.14922>
- 720 Kim, E., Gatebe, C., Hall, D., Newlin, J., Misakonis, A., Elder, K., Marshall, H. P., Hiem-
721 stra, C., Brucker, L., De Marco, E., Crawford, C., Kang, D. H., & Entin, J. (2017).
722 NASA's snowex campaign: Observing seasonal snow in a forested environment. *2017
723 IEEE International Geoscience and Remote Sensing Symposium (IGARSS)*, 1388–1390.
724 <https://doi.org/10.1109/IGARSS.2017.8127222>
- 725 Kobayashi, D. (1987). Snow accumulation on a narrow board. *Cold Regions Science and
726 Technology*, 13(3), 239–245. [https://doi.org/10.1016/0165-232X\(87\)90005-X](https://doi.org/10.1016/0165-232X(87)90005-X)
- 727 Kozak, A., & Kozak, R. A. (1995). Notes on regression through the origin. *Forestry Chronicle*,
728 71(3), 326–330. <https://doi.org/10.5558/tfc71326-3>
- 729 Langs, L. E., Petrone, R. M., & Pomeroy, J. W. (2020). A $\delta^{18}\text{O}$ and $\delta^2\text{H}$ stable water
730 isotope analysis of subalpine forest water sources under seasonal and hydrological stress
731 in the Canadian Rocky Mountains. *Hydrological Processes*, 34(26), 5642–5658. <https://doi.org/10.1002/hyp.13986>
- 733 Lehtonen, I., Kämärainen, M., Gregow, H., Venäläinen, A., & Peltola, H. (2016). Heavy snow
734 loads in Finnish forests respond regionally asymmetrically to projected climate change.
735 *Natural Hazards and Earth System Sciences*, 16(10), 2259–2271. <https://doi.org/10.5194/nhess-16-2259-2016>
- 737 Lumbrazo, C., Bennett, A., Currier, W. R., Nijssen, B., & Lundquist, J. (2022). Evalu-
738 uating multiple canopy-snow unloading parameterizations in SUMMA with time-lapse
739 photography characterized by citizen scientists. *Water Resources Research*, 58(6), 1–22.
740 <https://doi.org/10.1029/2021WR030852>
- 741 Lundberg, A., & Hallidin, S. (1994). Evaporation of intercepted snow: Analysis of governing
742 factors. *Water Resources Research*, 30(9), 2587–2598.

- 743 Lundquist, J. D., Dickerson-Lange, S., Gutmann, E., Jonas, T., Lumbrazo, C., & Reynolds, D.
744 (2021). Snow interception modelling: Isolated observations have led to many land surface
745 models lacking appropriate temperature sensitivities. *Hydrological Processes*, 35(7), 1–20.
746 <https://doi.org/10.1002/hyp.14274>
- 747 MacDonald, J. P. J. (2010). *Unloading of intercepted snow in conifer forests* (Master of
748 {{Science}}) August; pp. 0–93). University of Saskatchewan.
- 749 Moeser, D., Stähli, M., & Jonas, T. (2015). Improved snow interception modeling using
750 canopy parameters derived from airborne LiDAR data. *Water Resources Research*, 51(7),
751 5041–5059. <https://doi.org/10.1002/2014WR016724>
- 752 Musselman, K. N., Pomeroy, J. W., & Link, T. E. (2015). Variability in shortwave irradiance
753 caused by forest gaps: Measurements, modelling, and implications for snow energetics.
754 *Agricultural and Forest Meteorology*, 207, 69–82. <https://doi.org/10.1016/j.agrformet.2015.03.014>
- 755 Nock, C. A., Lecigne, B., Taugourdeau, O., Greene, D. F., Dauzat, J., Delagrange, S., &
756 Messier, C. (2016). Linking ice accretion and crown structure: Towards a model of the
757 effect of freezing rain on tree canopies. *Annals of Botany*, 117(7), 1163–1173. <https://doi.org/10.1093/aob/mcw059>
- 758 Pfister, R., & Schneebeli, M. (1999). Snow accumulation on boards of different sizes and
759 shapes. *Hydrological Processes*, 13(14-15), 2345–2355. [https://doi.org/10.1002/\(SICI\)1099-1085\(199910\)13:14/15%3C2345::AID-HYP873%3E3.0.CO;2-N](https://doi.org/10.1002/(SICI)1099-1085(199910)13:14/15%3C2345::AID-HYP873%3E3.0.CO;2-N)
- 760 Pomeroy, J. W., Brown, T., Fang, X., Shook, K. R., Pradhananga, D., Armstrong, R., Harder,
761 P., Marsh, C., Costa, D., Krogh, S. A., Aubry-wake, C., Annand, H., Lawford, P., He,
762 Z., Kompanizare, M., & Moreno, J. I. L. (2022). The cold regions hydrological modelling
763 platform for hydrological diagnosis and prediction based on process understanding. *Journal
764 of Hydrology*, 615(128711), 1–25. <https://doi.org/10.1016/j.jhydrol.2022.128711>
- 765 Pomeroy, J. W., Fang, X., & Ellis, C. R. (2012). Sensitivity of snowmelt hydrology in Marmot
766 Creek, Alberta, to forest cover disturbance. *Hydrological Processes*, 26(12), 1891–1904.
767 <https://doi.org/10.1002/hyp.9248>
- 768 Pomeroy, J. W., Marsh, P., & Gray, D. M. (1997). Application of a distributed blowing snow
769 model to a boreal forest. *Hydrological Processes*, 11(10), 1571–1588. [https://doi.org/10.1002/\(SICI\)1099-1085\(199710\)11:10/15%3C1571::AID-HYP100%3E3.0.CO;2-1](https://doi.org/10.1002/(SICI)1099-1085(199710)11:10/15%3C1571::AID-HYP100%3E3.0.CO;2-1)
- 770

- 772 model to the arctic. *Hydrological Processes*, 11(11), 1451–1464. [https://doi.org/10.1002/\(SICI\)1099-1085\(199709\)11:11%3C1451::aid-hyp449%3E3.0.co;2-q](https://doi.org/10.1002/(SICI)1099-1085(199709)11:11%3C1451::aid-hyp449%3E3.0.co;2-q)
- 773
- 774 Pomeroy, J. W., Parviainen, J., Hedstrom, N., & Gray, D. M. (1998). Coupled modelling of
775 forest snow interception and sublimation. *Hydrological Processes*, 12(15), 2317–2337. [https://doi.org/10.1002/\(SICI\)1099-1085\(199812\)12:15%3C2317::AID-HYP799%3E3.0.CO;2-X](https://doi.org/10.1002/(SICI)1099-1085(199812)12:15%3C2317::AID-HYP799%3E3.0.CO;2-X)
- 776
- 777 Pomeroy, J. W., & Schmidt, R. A. (1993). The use of fractal geometry in modelling intercepted
778 snow accumulation and sublimation. *Eastern Snow Conference*, 50, 231–239.
- 779
- 780 R Core Team. (2024). *R: A language and environment for statistical computing* [Manual]. R
Foundation for Statistical Computing.
- 781
- 782 Rittger, K., Raleigh, M. S., Dozier, J., Hill, A. F., Lutz, J. A., & Painter, T. H. (2020). Canopy
783 adjustment and improved cloud detection for remotely sensed snow cover mapping. *Water
Resources Research*, 56(6), n/a. <https://doi.org/10.1029/2019WR024914>
- 784
- 785 Roesch, A., Wild, M., Gilgen, H., & Ohmura, A. (2001). A new snow cover fraction parame-
786 terization for the ECHAM4 GCM. *Climate Dynamics*, 17(12), 933–946. <https://doi.org/10.1007/s003820100153>
- 787
- 788 Roth, T. R., & Nolin, A. W. (2019). Characterizing maritime snow canopy interception in
789 forested mountains. *Water Resources Research*, 55(6), 4564–4581. <https://doi.org/10.1029/2018WR024089>
- 790
- 791 Safa, H., Krogh, S. A., Greenberg, J., Kostadinov, T. S., & Harpold, A. A. (2021). Unraveling
792 the controls on snow disappearance in montane conifer forests using multi-site lidar. *Water
Resources Research*, 57(12), 1–20. <https://doi.org/10.1029/2020WR027522>
- 793
- 794 Satterlund, D. R., & Haupt, H. F. (1967). Snow catch by conifer crowns. *Water Resources
Research*, 3(4), 1035–1039. <https://doi.org/10.1029/WR003i004p01035>
- 795
- 796 Schmidt, R. A., & Gluns, D. R. (1991). Snowfall interception on branches of three conifer
797 species. *Canadian Journal of Forest Research*, 21(8), 1262–1269. <https://doi.org/10.1139/x91-176>
- 798
- 799 Schmidt, R. A., & Troendle, C. A. (1989). Snowfall into a forest and clearing. *Journal of
Hydrology*, 110(3-4), 335–348. [https://doi.org/10.1016/0022-1694\(89\)90196-0](https://doi.org/10.1016/0022-1694(89)90196-0)
- 800 Smith, C. D. (2007). Correcting the wind bias in snowfall measurements made with a Geonor

- 801 T-200B precipitation gauge and alter wind shield. *87th AMS Annual Meeting*.
- 802 Staines, J., & Pomeroy, J. W. (2023). Influence of forest canopy structure and wind flow
803 on patterns of sub-canopy snow accumulation in montane needleleaf forests. *Hydrological
804 Processes*, 37(10), 1–19. <https://doi.org/10.1002/hyp.15005>
- 805 Storck, P., Lettenmaier, D. P., & Bolton, S. M. (2002). Measurement of snow interception and
806 canopy effects on snow accumulation and melt in a mountainous maritime climate, Oregon,
807 United States. *Water Resources Research*, 38(11), 1–16. [https://doi.org/10.1029/2002wr 001281](https://doi.org/10.1029/2002wr
808 001281)
- 809 Troendle, C. A. (1983). The potential for water yield augmentation from forest management
810 in the rocky mountain region. *Journal of the American Water Resources Association*, 19(3),
811 359–373. <https://doi.org/10.1111/j.1752-1688.1983.tb04593.x>
- 812 Valante, F., David, J. S., & Gash, J. H. C. (1997). Modelling interception loss for two sparse
813 eucalypt and pine forests in central Portugal using reformulated Rutter and Gash analytical
814 models. *Journal of Hydrology*, 190(1-2), 141–162. [https://doi.org/10.1016/S0022-1694\(96 \)03066-1](https://doi.org/10.1016/S0022-1694(96
815)03066-1)
- 816 Van Stan, J. T., Siegert, C. M., Levia, D. F., & Scheick, C. E. (2011). Effects of wind-
817 driven rainfall on stemflow generation between codominant tree species with differing crown
818 characteristics. *Agricultural and Forest Meteorology*, 151(9), 1277–1286. [https://doi.org/10.1016/j.agrformet.2011.05.008](https://doi.org/
819 10.1016/j.agrformet.2011.05.008)
- 820 Varhola, A., Coops, N. C., Weiler, M., & Moore, R. D. (2010). Forest canopy effects on
821 snow accumulation and ablation: An integrative review of empirical results. *Journal of
822 Hydrology*, 392(3-4), 219–233. <https://doi.org/10.1016/j.jhydrol.2010.08.009>
- 823 Vionnet, V., Mortimer, C., Brady, M., Arnal, L., & Brown, R. (2021). Canadian historical
824 snow water equivalent dataset (CanSWE, 1928–2020). *Earth System Science Data*, 13(9),
825 4603–4619. <https://doi.org/10.5194/essd-13-4603-2021>
- 826 Watanabe, S., & Ozeki, J. (1964). Study of fallen snow on forest trees (II). Experiment on the
827 snow crown of the Japanese cedar. *Jap. Govt. Forest Exp. Sta. Bull*, 169, 121–140.
- 828 Wheeler, K. (1987). Interception and redistribution of snow in a subalpine forest on a storm-
829 by-storm basis. In *55th annual western snow conference*. Western Snow Conference.